Structural Requirements for Inhibition of the Neuronal Nitric Oxide Synthase (NOS-I): 3D-QSAR Analysis of 4-Oxo- and 4-Amino-Pteridine-Based Inhibitors

Hans Matter,*[,†] Peter Kotsonis,[‡,§] Otmar Klingler,[†] Hartmut Strobel,[†] Lothar G. Fröhlich,[‡] Armin Frey,[‡] Wolfgang Pfleiderer,[∥] and Harald H. H. W. Schmidt[‡]

Molecular Modeling, Aventis Pharma, G 878, 65926 Frankfurt am Main, Germany, Chemistry, Aventis Pharma, 65926 Frankfurt am Main, Germany, Rudolf-Buchheim-Institut of Pharmacology, University of Giessen, D-35392 Giessen, Germany, and Faculty of Chemistry, University of Konstanz, 78434 Konstanz, Germany

Received February 13, 2002

The family of homodimeric nitric oxide synthases (NOS I−III) catalyzes the generation of the cellular messenger nitric oxide (NO) by oxidation of the substrate L-arginine. The rational design of specific NOS inhibitors is of therapeutic interest in regulating pathological NO levels associated with sepsis, inflammatory, and neurodegenerative diseases. The cofactor (6*R*)-5,6,7,8-tetrahydrobiopterin (H_4Bip) maximally activates all NOSs and stabilizes enzyme quaternary structure by promoting and stabilizing dimerization. Here, we describe the synthesis and three-dimensional (3D) quantitative structure−activity relationship (QSAR) analysis of 65 novel 4-amino- and 4-oxo-pteridines (antipterins) as inhibitors targeting the H_4Bip binding site of the neuronal NOS isoform (NOS-I). The experimental binding modes for two inhibitors complexed with the related endothelial NO synthase (NOS-III) reveal requirements of biological affinity and form the basis for ligand alignment. Different alignment rules were derived by building other compounds accordingly using manual superposition or a genetic algorithm for flexible superposition. Those alignments led to 3D-QSAR models (comparative molecular field analysis (CoMFA) and comparative molecular similarity index analysis (CoMSIA)), which were validated using leave-one-out cross-validation, multiple analyses with two and five randomly chosen cross-validation groups, perturbation of biological activities by randomization or progressive scrambling, and external prediction. An iterative realignment procedure based on rigid field fit was used to improve the consistency of the resulting partial least squares models. This led to consistent and highly predictive 3D-QSAR models with good correlation coefficients for both CoMFA and CoMSIA, which correspond to experimentally determined NOS-II and -III H_4Bip binding site topologies as well as to the NOS-I homology model binding site in terms of steric, electrostatic, and hydrophobic complementarity. These models provide clear guidelines and accurate activity predictions for novel NOS-I inhibitors.

1. Introduction

Nitric oxide synthases (NOS[1]) are the only heme-containing enzymes that require (6*R*)-5,6,7,8-tetrahydrobiopterin (H_4Bip) as cofactor for maximal activation. All three known isoforms[2] catalyze oxidation from the substrate L-arginine[3] to L-citrulline and nitric oxide (NO) or a related N-oxide.[4] NO is an important modulator of physiological and pathophysiological function in the cardiovascular, neuronal, and immune system,[5,6] and it is involved as an intercellular signal and defensive cytotoxin in the nervous, muscular, cardiovascular, and immune systems.[5] While the neuronal NOS (NOS-I) and endothelial NOS (NOS-III) isoforms produce low NO concentrations, the cytokine inducible NOS (NOS-II) is a high-output system that synthesizes larger NO concentrations to counter pathogens and coordinate T-cell responses. The native enzyme is homodimeric; each subunit contains a catalytic N-terminal oxygenase domain (residues 1−498) and a C-terminal electron-supplying reductase domain (residues 531−1144). The oxygenase domain binds heme, H_4Bip, and L-arginine.[7,8] Dimerization and H_4Bip binding are essential for catalytic activity. Interestingly, only the fully reduced form of H_4Bip can support NO production.[9] The binding of calmodulin to NOS promotes electron flow from the reductase to the oxygenase domain.[10]

Although similar in their catalytic mechanism, the NOS isoforms are distinguished by their regulation and localization. The neuronal (NOS-I) and endothelial (NOS-III) isoforms are present constitutively; they are dependent on elevated free intracellular Ca^{2+} concentrations to interact with calmodulin. NOS-I is localized in neuronal tissue,[11] skeletal muscle, and epithelial cells and modulates neurotransmission, gastrointestinal motility, penile erection, etc.[5b] Experiments using NOS-I knockout mice and the NOS-I selective inhibitor 7-nitroindazole[12] indicate a role for NOS-I in stroke,[13] Parkinson's disease,[14] and pain.[15] NOS-III, found in vascular endothelial cells[16] regulating blood pressure and hemostasis, is not a therapeutic target for pharmacological intervention given its role in maintaining blood flow. The inducible isoform (NOS-II) is expressed in macrophages and other cells upon exposure to cytokines and plays a key role in early immune responses

* To whom correspondence should be addressed. Tel.: ++49-69-305-84329. Fax: ++49-69-331399. E-mail: hans.matter@aventis.com.
† Chemistry, Aventis Pharma.
‡ University of Giessen.
§ Current address: Novartis Institute for Medical Sciences, 5 Gower Place, London, WC1E 6BN, U.K.
∥ University of Konstanz.

10.1021/jm020074g CCC: $22.00
Published on Web 05/25/2002

as a cytotoxic agent[17,18] against bacteria, viruses, and other pathogens. Its activity does not depend on elevations in the free intracellular Ca^{2+}, since it already binds calmodulin at Ca^{2+} levels of resting cells. Overexpression of NOS-II has been associated with tissue damage and severe hypotension in disease states such as sepsis.

Comparing human NOS genes reveals an isoform sequence homology of 50%, suggesting that they may differ from each other in regulatory aspects.[19] X-ray structures for dimeric NOS-II[7] and NOS-III[8] reveal structurally conserved H_4Bip binding sites,[20] which differ from the corresponding binding sites in monomeric X-ray structures[21] and thus explain the need for dimerization for activity. Both binding sites in dimeric X-ray structures were identical, no preferential binding of H_4Bip was reported.[8] In this study, these dimeric X-ray structures were used for homology modeling of NOS-I. This homology model was used only for validation of the consistency of the ligand-derived three-dimensional (3D) quantitative structure−activity relationship (QSAR) models by interpretation in combination with binding site requirements, as the lack of a NOS-I X-ray structure requires a ligand-based approach to understand structural requirements for NOS inhibition rather than a structure-based approach.

The rational design of isoform specific NOS inhibitors is of great pharmacological interest to reduce pathologically elevated NO synthesis implicated in disease states such as sepsis,[22] inflammation, and neurodegeneration stroke.[1] Prototypical NOS inhibitors were analogues of L-arginine,[23] e.g., N^{ω}-methyl-L-arginine (L-NMA[24]), N^{ω}-methyl-L-argininemethylester (L-NMMA), N^{ω}-nitro-L-arginine (L-NNA[25]), N^{δ}-iminoethyl-L-orthinine (L-NIO[26]), and N^{ω}-nitro-L-arginine-containing dipeptide amides.[27] They show minimal isoform selectivity except for dipeptide amides, and more recently, some peptidomimetics[28] interfere with other arginine-based biological pathways. Although L-citrulline does regulate NOS activity, analogues of L-citrulline, e.g., L-thiocitrulline (L-TC), L-homothiocitrulline (L-HTC), and S-methyl-L-thiocitrulline (L-SMTC),[29] are potent inhibitors.[30] These compounds compete with L-arginine and show a favorable toxicity profile[16,11] in animal models. In addition, nonpeptide inhibitors with variable isoform selectivity were described.[31,32] Other binding sites have also been targeted,[30,33] including those associated with flavins, heme, and calmodulin binding.

Our previous work on NOS-I inhibitors led to a class specifically targeting the H_4Bip binding site (antipterins).[34−36] Two chemical series based on a 4-amino-[34,35] or 4-oxo-pteridine scaffold[36] were systematically varied at the 2-, 4-, 5-, 6-, and 7-positions to derive a SAR. In the present study, a set of 65 4-oxo and 4-amino pteridines was analyzed using 3D-QSAR techniques to derive predictive models for further inhibitor design. The lack of a NOS-I X-ray structure prompted us for a ligand-based design and analysis approach using 3D-QSAR to obtain information directed toward design of novel analogues. The known X-ray structures of related NOS isoforms[7,8] were used to derive an alignment hypothesis for 3D-QSAR using two of our inhibitors in their experimental binding mode from NOS-III X-ray structures.[36] The ligand-based approach was carefully validated and checked for internal consistency; hence, chemical interpretations are significant and justified. The homology model of NOS-I, however, was used to support the initial alignment hypothesis and to interpret ligand-derived requirements for NOS-I affinity from 3D-QSAR studies, providing a structural basis that accounts for key ligand−enzyme interactions. It provides a consistency check for chemical interpretation, while the QSAR model itself is based only on structural information present in the set of NOS-I inhibitors.

To establish the SAR of these inhibitors, different ligand-based 3D-QSAR methods were employed. Comparative molecular field analysis (CoMFA)[37−39] and comparative molecular similarity index analysis (CoMSIA)[40] were used to correlate molecular property fields of aligned inhibitors to NOS-I biological activities using the PLS method (partial least squares).[41] Cross-validation[42] was used to check for consistency and predictiveness. An iterative realignment procedure based on rigid field fit to average CoMFA fields was used to improve the consistency of PLS models. The resulting contour maps from 3D-QSAR models enhance our understanding of electrostatic, hydrophobic, and steric requirements for ligand binding and provide a guide for the design of novel pteridine-based NOS inhibitors to those regions, where structural variations altering steric or electrostatic fields reveal a significant correlation to biological properties.

2. Methods

2.1. Chemistry. All 65 compounds used for the 3D-QSAR analyses were synthesized using procedures previously described or given in the Experimental Section. The data set is well-balanced and contains different chemical functionalities. All chemical structures and biological activities are listed in Table 1. The best IC_{50} value is significant for targeting the H_4Bip binding site, while the split of 2 orders of magnitude is relevant to draw significant conclusions from this QSAR study.

2.2. Computational Procedure. 2.2.1. General Procedure. All modeling studies were performed using the program SYBYL[43] on Silicon Graphics workstations. A number of procedures were automated using SPL (Sybyl Programming Language). Energy calculations were based on the TRIPOS 6.0 force field[44] with Gasteiger−Marsili charges.[45] Ligands and protein−ligand complexes were minimized using the quasi-Newton−Raphson (BFGS) procedure. Ligand geometries were optimized using MOPAC 6.0[46] and the AM1 Hamiltonian,[47] which yields atomic partial charges for computing electrostatic fields.

For homology modeling and docking of reference compounds, the X-ray structures of endothelial and inducible NOS isoforms (NOS-II, NOS-III)[7,8] were obtained from the protein data bank (PDB).[48] All hydrogen atoms were added, while conserved structural water and a glycerol molecule close to the H_4Bip site were deleted. Protein structures were aligned using the Cα atoms of related amino acids around the H_4Bip binding site plus selected heavy atoms from heme and H_4Bip frameworks.

After analysis of protein−ligand interactions using the program GRID,[49] some reference molecules were manually docked into the H_4Bip binding site. Then, the resulting complex was minimized while treating all protein residues within a sphere of 4 Å around the

Table 1. Sixty-Five 4-Oxo and Four Amino-pteridines as NOS-I Inhibitors Used in This Study

a)

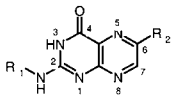

I

ID	R_1	R_2	IC_{50} (μM)
1	H	$HOCH_2$	180.0
159	H	p-$N_3C_6H_4COOCH_2$	125.0
162	H	p-$N_3C_6H_4$	46.0
163	$(CH_3)_2CHCO$	p-$N_3C_6H_4$	42.0
167	H	$C_6H_5OCH_2$	63.0
176	H	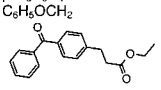	60.0
183	H	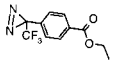	44.0
261	H	C_6H_5	26.0
268	H		21.0
339	H	p-FC_6H_4	8.0
341	H		8.0
342	H		29.0
5	H	CH_3SCH_2	88.0
6	H	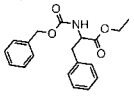	38.0
7	H	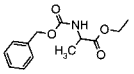	130.0

b)

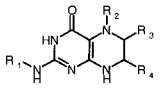

II

ID	R_1	R_2	R_3	R_4	IC_{50} (μM)
150	H	p-$N_3C_6H_4CO$	p-$N_3C_6H_4COOCH_2$	H	28.0
177	$(CH_3)_2CHCO$	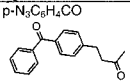	H	H	190.0
179	H	H	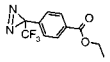	H	42.0
187	H	H	C_6H_5	H	7.3
189	CH_3	H	H	H	650.0
213	H	H	$CH_3(CH_2)_9OCH_2$	H	81.0
149	H	C_6H_5CO	$C_6H_5COOCH_2$	H	172.0
27	H	H	H_2NCH_2	H	32.0
28	H	H	CH_3NHCH_2	H	20.0
29	H	H	$(CH_3)_2NCH_2$	H	25.0
33	H	H	$CH_3SO_2CH_2$	H	40.0
52	H	C_6H_5NHCS	H	H	50.0
56	H	C_6H_5CO	H	H	90.0
72	$(CH_3)_2CHCO$	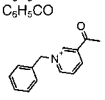	C_6H_5	C_6H_5	16.0

c)

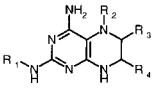

III

ID	R_1	R_2	R_3	R_4	IC_{50} (μM)
185	H	H	C_6H_5	H	6.0
186	H	H	H	C_6H_5	24.0
194	CH_3	H	C_6H_5	C_6H_5	30.0
195	H	HCO	H	H	300.0
203	H	H	$CH_3CHOHCHOH$	H	9.0
214	H	H	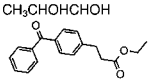	H	48.0

d)

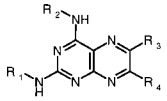

IV

ID	R_1	R_2	R_3	R_4	IC_{50} (μM)
199	H	H	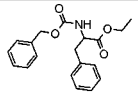	H	180.0

ID	R_1	R_2	R_3	R_4	IC_{50} (μM)
215	H	H	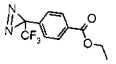	H	140.0
225	$(CH_3)_2CHCO$	$(CH_3)_2CHCO$	C_6H_5	C_6H_5	94.0
227	H	$(CH_3)_2CHCO$	C_6H_5	C_6H_5	192.0
13	H	H	$CH_3(CH_2)_9OCH_2$	H	30.0

e)

ID	structure	IC_{50} (μM)
201	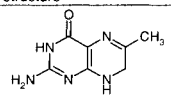	145.0
200	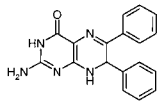	30.0
32	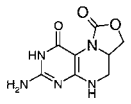	40.0

f)

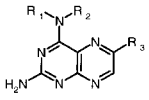

V

ID	$R_{1,2}$	R_3	IC_{50} (μM)
246	CH_3	p-$CH_3C_6H_4$	75.0
247	CH_3	p-$CH_3OC_6H_4$	74.0
301	CH_3CH_2	p-$CH_3OC_6H_4$	40.0
303	$C_6H_5CH_2$	C_6H_5	3.0
305	$C_6H_5CH_2$	p-$CH_3OC_6H_4$	4.0
306	$C_6H_5CH_2$	3,4-$(CH_3O)_2C_6H_3$	2.0
310	$CH_3CH_2CH_2$	3,4-$(CH_3O)_2C_6H_3$	39.0

g)

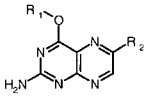

VI

ID	R_1	R_2	IC_{50} (μM)
264	$CH_3(CH_2)_4$		8.0
265	$CH_3(CH_2)_4$		13.0
270	$CH_3(CH_2)_4$	$C_6H_5COCH_2S$	11.0

h)

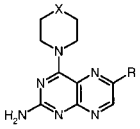

VIII

ID	X	R	IC_{50} (μM)
311	O	C_6H_5	82.0
313	O	p-$CH_3OC_6H_4$	34.0
315	CH_2	C_6H_5	30.0
317	CH_2	p-$CH_3OC_6H_4$	60.0
318	CH_2	3,4-$(CH_3O)_2C_6H_3$	44.0

i)

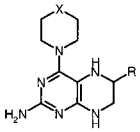

IX

ID	X	R	IC_{50} (μM)
328	CH_2	p-ClC_6H_4	13.0
329	CH_2	p-$CH_3OC_6H_4$	42.0
330	CH_2	C_6H_5	6.0

j)

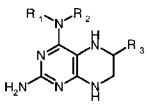

X

ID	R_1	R_2	R_3	IC_{50} (μM)
332	$CH_3CH_2CH_2$	$CH_3CH_2CH_2$	p-$CH_3OC_6H_4$	34.0
334		H	p-ClC_6H_4	5.0
333	CH_3CH_2	CH_3CH_2	p-ClC_6H_4	8.0
35	H	H	$CH_3CH_2OCH_2$	30.0

ligand as flexible. Convergence criteria were set to 0.001 kcal/Å. Some related compounds were built accordingly, docked into the NOS-III H_4Bip binding site, and minimized using such a partially flexible receptor. However, the resulting binding modes were only used qualitatively, while 3D-QSAR results using the ligand-based approach described below were applied to obtain detailed insights into the SAR of this chemical series.

The program MOLCAD[50] was used to visualize protein−ligand interactions by mapping properties such as lipophilicity[51,52] and electrostatic potential (obtained using the Poisson−Boltzmann equation[53]) onto solvent accessible surfaces.[54] The step width for the grid to compute the Poisson−Boltzmann electrostatic potential was set to 1 Å, while the border width of the solvent grid around the molecule was set to 8 Å. Dielectric constants of 80 for the solvent and 2 for the solute were used. The electrostatic potential at the boundary was computed using the Debye−Hückel equation.

2.2.2. Homology Modeling. A homology model for NOS-I was generated to obtain more information about H_4Bip binding site differences using the program Composer.[55] The structures of dimeric NOS-III and NOS-II (PDB codes 1nod, 2nod, 3nod, 1nse, 3nse, 4nse[7,8]) served as input homologue sequences. For loop searching, the Sybyl 6.5 binary version of the PDB database with 1495 nonredundant protein structures was used. A multiple alignment on homologous sequences was generated, and identities across all sequences were assigned weights proportional to the square of their percentage sequence identity to the model sequence. The weights determine the relative contribution of each homologue to the framework on which the model was built.[56] Then, a structural alignment of their 3D structures using seed residues as starting points was performed, leading to the determination of structurally conserved regions (SCRs). The unknown sequence (human brain NOS-I, GenBank accession code L02881) was aligned with the SCRs to determine the location of the SCRs in the target sequence and the homologue to use in constructing the backbone of each SCR in the final model. This led to a model of the SCRs of the target protein. A fragment from one of the homologues was used to model the backbone of each SCR, while a rule-based procedure was employed to model side chains. Finally, the structurally variable regions of the target protein were constructed by selecting a fragment to model each loop region either from the corresponding location in a homologous protein or from the entire protein database. The final NOS-I monomer was checked for steric overlap, superimposed onto other isoforms, and completed by adding heme, H_4-Bip, and another NOS-I monomer according to the NOS-III and NOS-II dimerization pattern. Finally, the H_4Bip/NOS-I dimer model was minimized treating H_4Bip, heme, and all binding site residues within a sphere of 4 Å as flexible.

2.2.3. Alignment as Basis of 3D-QSAR. Three different alignment rules were used for 3D-QSAR studies of this set of 65 NOS-I inhibitors. The first alignment (A) was based on an atom-based rmsd fit using the pteridine scaffold. This was found a reasonable approach, as X-ray structure data[36] of the related isoform NOS-III in complex with the herein used inhibitors 32 and 185[36] revealed a common orientation of the 4-oxo[36] and 4-amino[35] series. Interestingly, the oxygen and nitrogen atoms at C4 and C2 of the bicyclic scaffold adopt similar orientations; they are involved in similar direct or water-mediated hydrogen-bonding interactions to the NOS-III binding site (Figure 1A). All other inhibitors were manually built analogous to X-ray structures in the Cambridge crystallographic database (CSD)[57] and by systematic searching to identify minimum conformations. Dihedral angles without CSD entry were adjusted using canonical rules. Finally, all compounds were optimized with MOPAC 6.0[46,47] and superimposed onto the pteridine framework, producing alignment A1.

Alignment B was obtained using GASP,[58] a genetic algorithm for flexible molecular overlay. Its fitness function is a weighted combination of the number and similarities of superimposed features, the overlay volume integral plus internal van der Waals energies. Except for a maximum of 300 000 GA operations, default parameters were utilized. Several superpositions were generated using either compound **303** from the substituted 4-amino series or H_4Bip as rigid template and compounds **185**, **187**, **261**, and **341** as flexible candidates. The 10 models with the best fitness function from each run of the GA were analyzed. They all had in common that the bicyclic scaffold of substituted 4-amino compounds was shifted relative to the 4-oxo and unsubstituted 4-amino scaffolds (Figure 1). All remaining molecules were superimposed using an atom-based rmsd fit of the bicyclic scaffold for individual series, leading to alignment B1.

After initial PLS analyses for alignments A1 and B1, an iterative realignment procedure was applied to compounds with high absolute residuals to improve the consistency of 3D-QSAR models. As steric CoMFA interaction energies are usually computed using a Lennard−Jones 6−12 potential with a steep increase in energy at short distances, significant energy differences are observed at individual grid points comparing two molecules, which are not perfectly aligned. To account for this situation, a rigid-body field fit was applied for realigning molecules with absolute residuals >0.5. Any new orientation was accepted, if the prediction of the biological activity was improved. A rigid-body field fit minimizes the rms differences in the sum of steric and electrostatic interaction energies between a compound and a template field with respect to six rigid-body degrees of freedom.[37] Here, the averaged steric and electrostatic fields for all molecules were used. This procedure, related to another approach,[59] improves the statistical quality of the initial PLS model significantly, while it requires careful validation. This realignment followed by another PLS analysis was applied three times starting from the PLS results of alignment A1 producing alignments and analyses A2, A3, and A4. The same procedure applied to alignment B1, which produced B2, B3, and B4, respectively.

Alignment C1 was obtained using a flexible field fit[38] of all molecules in alignment A1 onto their averaged steric and electrostatic fields. The flexible fit uses field fit penalty terms E_{sff} and E_{eff} for steric and electrostatic potentials, respectively, added to the Tripos 6.0 force field.[44] A careful balance of those terms is crucial to avoid geometries with high residual strain. Thus, a

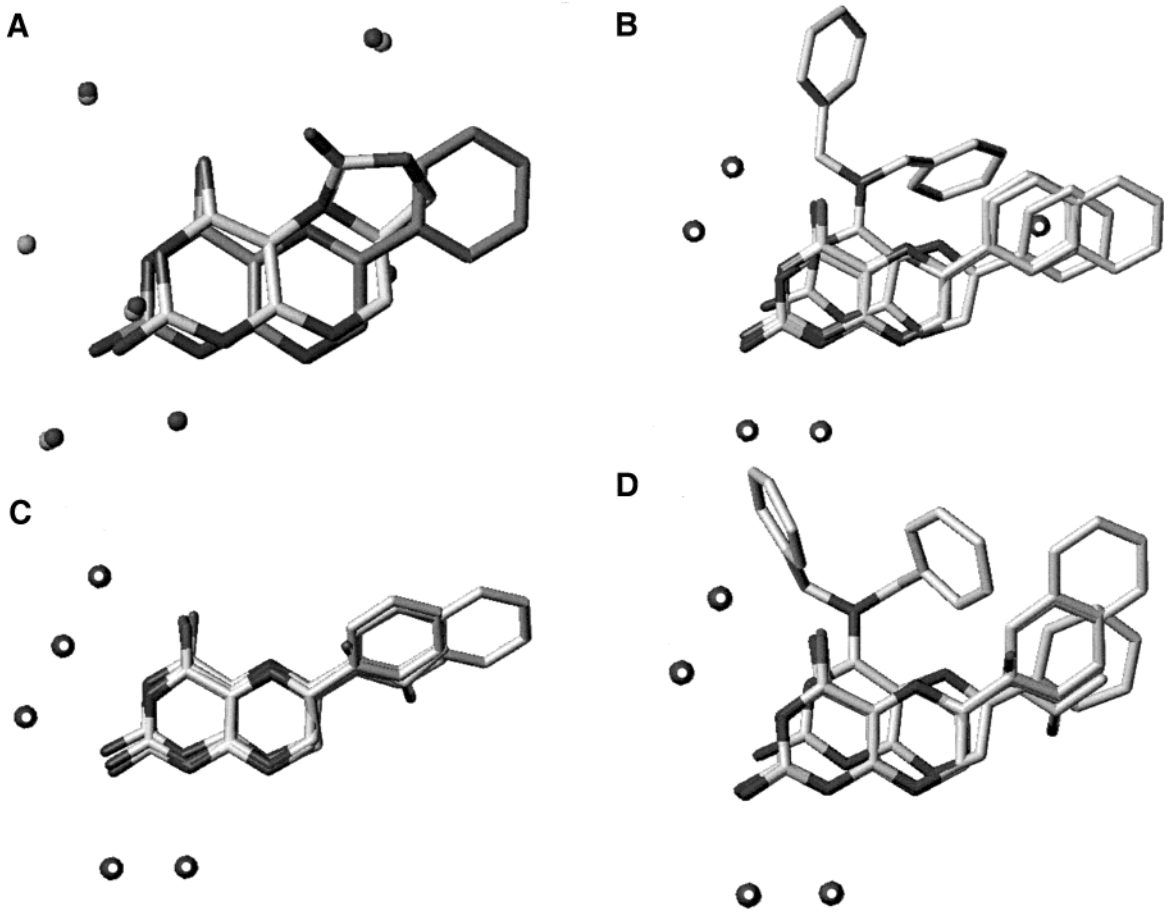

Figure 1. (A) X-ray structure-based alignment for **32** (4-oxo series: white carbons, dark water) and **185** (4-amino: gray carbons, gray water) in complex with NOS-III. (B) Best GASP alignment for 4-amino, 4-oxo, and substituted 4-amino series using **303** as rigid template and **185**, **187**, **261**, and **341** for flexible overlay. Pharmacophoric interaction sites are indicated by black circles. (C) Best GASP alignment using H_4Bip as rigid template, omitting **303** from the overlay set. (D) Best GASP alignment using H_4Bip as rigid template, including **303**.

moderate force constant of 0.5 kcal/mol was applied. Similar weights were assigned to all grid points, although improved results with individual weighting were reported.[60] Subsequently, applying the rigid realignment procedure produced alignments C2 and C3. Finally, an unconstrained energy minimization was used to relax every molecule from internal strain, producing alignment C4.

For each of those 12 individual alignments from three different classes, a CoMFA model and two CoMSIA models were generated, with and without hydrophobic field contributions. Each model was subjected to extensive statistical validations given below.

2.2.4. 3D-QSAR Studies. Steric and electrostatic interaction energies between a probe atom and aligned molecules are calculated at predefined grid points using a volume-dependent lattice with 2 Å spacing, a positively charged carbon atom, and a distance-dependent dielectric constant. The magnitude of the regions was defined to extend the conformers by 4.0 Å along the principal axes. Maximum field values were truncated to 30 kcal/mol for steric and ±30 kcal/mol for electrostatic energies. For points "inside" a molecule (steric energy of 30 kcal/mol), no electrostatic energy was computed. Those values were set to the mean of the related column.

This alignment served to compute steric, electrostatic, and hydrophobic similarity index fields for CoMSIA. The latter field description is based on Crippen's partial atomic hydrophobicities.[52] The advantage of CoMSIA fields is that no singularities occur at atomic positions due to a Gaussian type distance dependence of the physicochemical properties; thus, no arbitrary cutoffs are required. Similarity indices[61] were computed using a probe with charge +1, a radius of +1, a hydrophobicity of +1, and 0.3 as attenuation factor α for the Gaussian type distance dependence.

Equal weights for CoMFA or CoMSIA fields were assigned using the CoMFA STD scaling option.[62] Enzyme inhibition is expressed as $\log(1/IC_{50} \cdot 100\,000)$. Cross-validated analyses were run using the leave-one-out method in SAMPLS[63] or two and five cross-validation groups with random selection of group members. PLS analyses using two or five randomly selected cross-validation groups were averaged over 100 runs. For CoMFA, columns with a variance smaller than 2.0 were excluded prior to the PLS analysis (minimum-σ). The overall quality of all PLS analyses was expressed using the cross-validated r^2 value r^2(cv).

For additional validation, all biological activities were randomized[64] 100 times and subjected to PLS analysis, and the mean cross-validated r^2 was calculated. As simple randomization of activities could be misleading, if there is appreciable redundancy in the data set, progressive scrambling[65] was used as an alternative randomization technique as well. This *y*-block perturba-

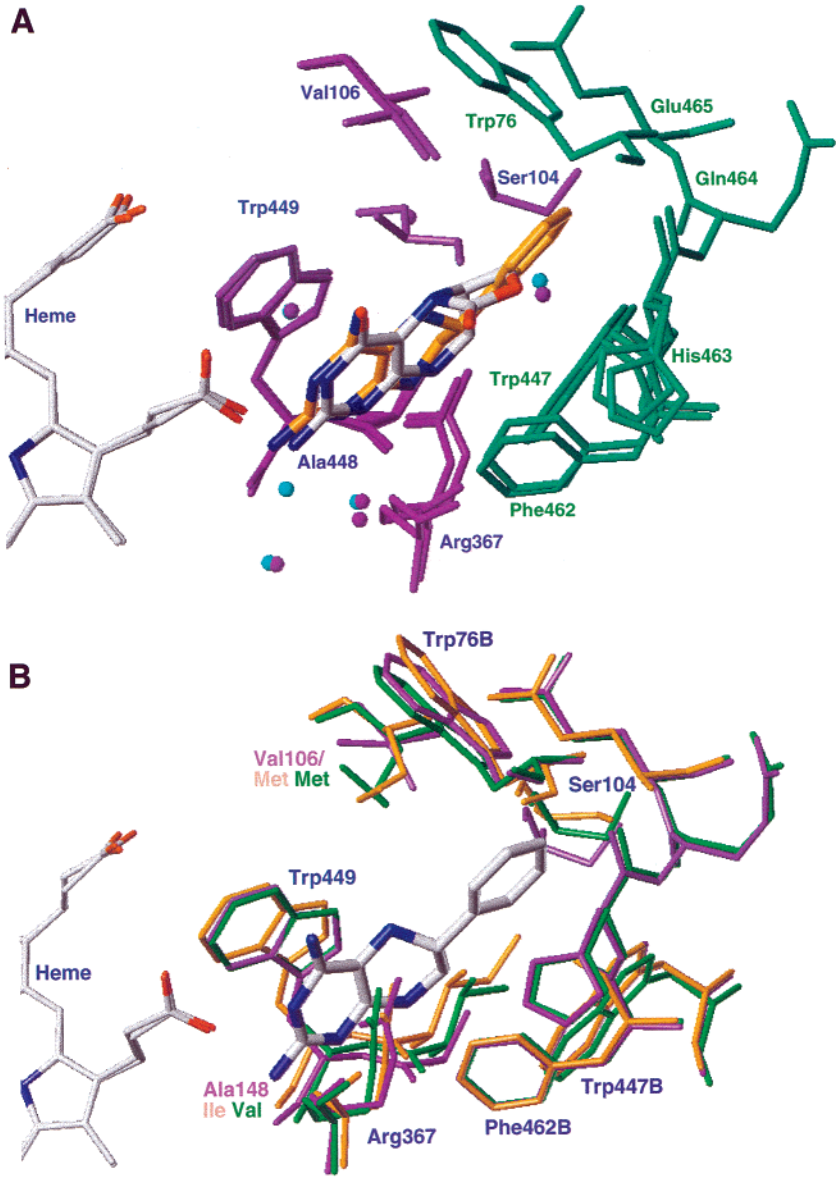

Figure 2. (A) Superposition of NOS-III inhibitor binding sites for **32** (white carbons) and **185** (orange carbons). Purple residues indicate the first NOS-III monomer, while green residues indicate the second monomer, showing that the binding site is located at the interface of both monomeric subunits. Both inhibitors are buried in the interior; they are oriented proximal and perpendicular to a heme. (B) Structural comparison of three NOS isoforms with the inhibitor **185**. The NOS-III binding site (PDB: 1nse) is shown in purple, NOS-II residues (PDB: 2nod) are shown in orange, and residues for the NOS-I homology model are displayed in green. Residue numbering is taken from NOS-III; differences to NOS-II and NOS-I are indicated.

tion strategy first subdivided biological activities into 2−12 subgroups of similar ranges. Subsequently, the biological activities were randomized only within a subgroup, while the relation between individual subgroups remained unaffected. Thus, the stability of each obtained regression model could be directly tested. Having 12 subgroups, only a small, local perturbation of biological activities was probed, while for two subgroups, a much larger portion of the data set is randomized. This method provides information about the structure of the *y*-block, indicates inconsistencies, and helps to estimate the tolerable error in biological activities for any PLS model. For analysis, the number of subgroups was plotted on the *x*-axis against the mean cross-validated r^2 value per submodel (20 randomizations each) on the *y*-axis.

3. Results

3.1. Binding Mode of Pterin-Based Derivatives.

The experimental alignment of the 4-oxo and 4-amino series in complex with NOS-III[36] as basis for alignment A1 is displayed in Figure 1A. The 4-amino inhibitor **185**[35] is shown with white carbons and black water molecules, while **32**[36] from the 4-oxo series is shown with gray carbons and gray water molecules. This alignment is based on H_4Bip binding site residues. Both ligands share a common orientation of the bicyclic framework, while the attached heteroatoms are involved in direct or water-mediated hydrogen bonds to the binding site. The inhibitors are deeply buried in the interior of the cavity and not accessible to bulk solvent, and they are oriented proximal and perpendicular to the heme molecule. In Figure 2A, both NOS-III X-ray

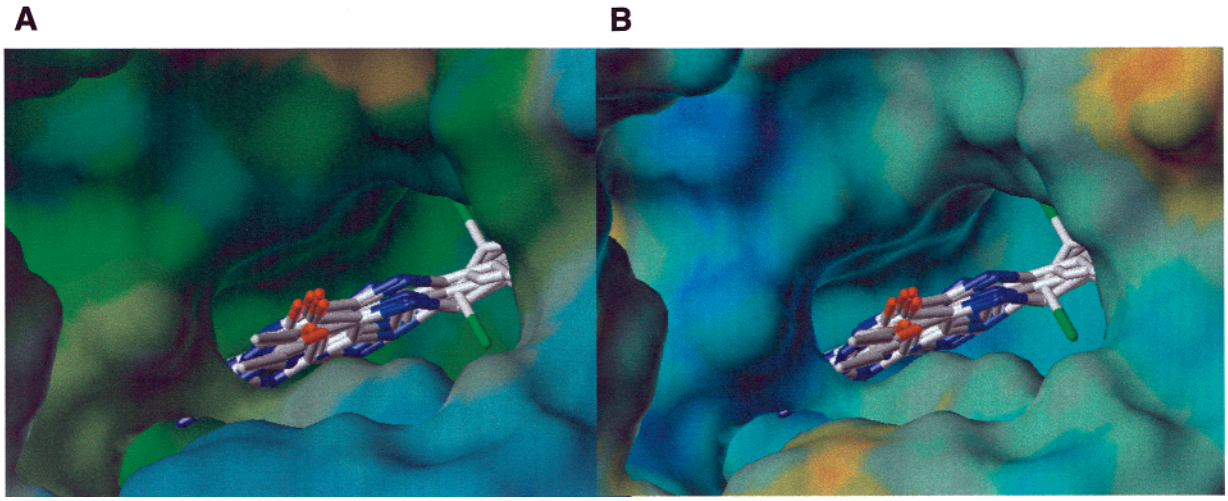

Figure 3. Connolly surface for NOS-II H_4Bip binding cavity based on the NOS-II X-ray structure (PDB file: 1nse) and best docking modes for the 10 most active NOS-I inhibitors. Different properties are mapped onto this surface using MOLCAD. (A) Lipophilic potential (brown, lipophilic; green, intermediate range; blue, hydrophilic). (B) Electrostatic potential based on Poisson−Boltzmann equation (red, negative; blue, positive).

structures with **185** and **32** are shown with purple residues for the first NOS monomer and green for the second, respectively. The main protein−ligand interaction occurs between the aromatic rings in both the inhibitors and the Trp449 indole. Both rings are stacked with a 3.6 Å distance, a motif present in other pterin−protein complexes.[66] The hydrogen-bonding pattern corresponds to H_4Bip bound to NOS-II and NOS-III.[7,8] The 4-amino-5,6,7,8-tetrahydropteridine is hydrogen-bonded to a heme carboxylate (O4/N4 via solvent, N3 directly), while the next potential partner for N5, a water molecule, is within a 4.1 Å distance. The structurally conserved water between the C4 substituent and the heme carboxylate is located at the same position, suggesting a similar hydrogen bond interaction. The carbamate carbonyl oxygen of **32** is hydrogen-bonded to Arg367 guanidine, while for **185** this group points toward the 4-amino function but does not provide an optimal geometry for interaction. For the NOS-II monomer, this part is disordered, explaining that only dimeric NOS with properly oriented Arg367 is able to bind H_4-Bip. The entrance region into the H_4Bip binding region is occupied by a glycerol molecule, while structural water molecules are displayed as spheres. The 2-amino-nitrogen in all molecules interacts via solvent with the heme carboxylate and with the backbone carbonyl group of Trp449, while nitrogen N1 in **185** and **32** is not involved in any hydrogen bond interaction but close to Trp449-CαH (2.14 Å). Finally, N8 is in close hydrogen-bonding contact to the carbonyl group of Ala448. The **185** hydrophobic phenyl side chain attached to C6 occupies a pocket formed by the side chains of Val106, TrpB447, TrpB076, and other backbone amide bonds, while this space is not occupied in the **32**/NOS-III complex. Val106 is replaced by Met for NOS-II and also NOS-I. This pocket is also occupied by the H_4Bip dihydroxypropyl chain, which also interacts with the Ser104 carbonyl oxygen and thus orients the cofactor within the binding site. This extended hydrogen-bonding network explains the high affinity of this cofactor (K_d 20 nM[67]).

A structural comparison of all three isoforms is shown in Figure 2B with the potent NOS-I inhibitor **185**. The NOS-III binding site (PDB file 1nse) is shown in purple, NOS-II residues (PDB file 2nod) are shown in orange, and residues for the NOS-I homology model are displayed in green. Residue numbering is taken from NOS-III. This comparison reveals two sequence differences for this inhibitor binding site: Val106/Met/Met and Ala148/Ile/Val (NOS-III/II/I). This suggests that experimental binding modes from other isoforms provide reasonable models for NOS-I binding.

Three similar alignments of the 4-amino, 4-oxo, and N-substituted 4-amino series generated using the program GASP are given in Figure 1B−D. The superposition in Figure 1B was generated using **303** from the 4-amino series as a rigid template and **185**, **187**, **261**, and **341** as candidates for flexible overlay. In general, the 10 best alignments from this and all other runs are very similar. Interestingly, substituted 4-amino compounds are not directly superimposed onto the 4-oxo and unsubstituted 4-amino scaffold. Black circles in Figure 1B−D indicate common pharmacophoric interaction sites (donor sites, acceptor sites, or hydrophobic regions) for each model. The superposition in Figure 1C was generated using H_4Bip as a rigid template, and **303** was omitted, leading to a direct superposition of all remaining molecules. One additional pharmacophoric interaction site in the area left to the N3 nitrogen is observed, while the hydrophobic interaction site of the substituents at C6 is missing. The final alignment was again based on H_4Bip as the template, but now including **303**, again showing the slight shift in the alignment of substituted 4-amino compounds. On the basis of these alignments, all remaining molecules were superimposed using heavy atom-based rmsd fitting of the bicyclic scaffold of corresponding series, leading to alignment B1.

Furthermore, 10 inhibitors were docked into the NOS-III binding site after manually orienting the bicyclic scaffold, which seems reasonable given the high structural similarity between different isoforms (Figure 2B). All residues and heme in a radius of 4 Å around ligands were treated flexible during minimization. The alignment after optimizing protein−ligand interactions for those 10 molecules is shown in Figure 3, supporting the

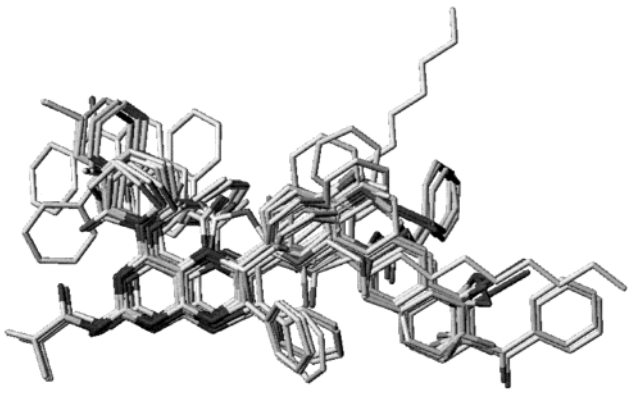

Figure 4. Superposition of 65 NOS-I inhibitors after iterative realignment used to derive the final PLS model C3 discussed for chemical interpretation.

atom-based alignment A1. These docking results also reveal that bulky substituents at C4 are unfavorable for the water-mediated hydrogen bond to one heme carboxylate. The NOS-III protein cavity with all superimposed inhibitors is shown in Figure 3 with its lipophilic potential (panel A: brown, lipophilic; green, intermediate range; blue, hydrophilic) and its electrostatic potential based on the Poisson−Boltzmann equation (panel B: red, negative; blue, positive) mapped onto the Connolly surface.

3.2. 3D-QSAR Analysis Using CoMFA. The superposition of all NOS-I inhibitors after iterative realignment is shown in Figure 4 for model C3, while superpositions for A4 and B4 are given in the Supporting Information, respectively. All 3D-QSAR models were based on $\log(1/IC_{50} \cdot 100\,000)$ as the dependent variable, MOPAC AM1 charges, and a grid spacing of 2 Å, leading to 2431 *X*-block columns per interaction field. The resulting PLS models using CoMFA or CoMSIA show a high degree of internal consistency. The CoMFA statistical results based on all three alignments A−C are summarized in the Supporting Information. For all 12 models, four significant components after PLS analysis were sufficient. For the atom-based alignment A1, a CoMFA model with an r^2(cv) value of 0.480 for four relevant PLS components and a conventional r^2 of 0.776 were obtained. The internal model consistency was improved using the iterative realignment procedure (keyword "rig-ffit1" in Supporting Information). After three realignments using the average steric and electrostatic fields from the previous PLS model, r^2(cv) values of 0.517, 0.538, and finally 0.575 were observed, respectively, while the conventional r^2 values for these models were 0.844, 0.865, and finally 0.885. All four PLS models resulted in a similar chemical interpretation, when analyzing CoMFA SD*Coeff maps. They show between 62 and 68% steric field contributions, while the importance of electrostatic interactions for predictive models is only 33−38%.

For alignment B1 based on GASP, an initial CoMFA model with an r^2(cv) value of 0.511 and a conventional r^2 of 0.830 was obtained. Also for this model, the internal consistency was improved using iterative realignment (Table S1 of Supporting Information). Three realignment steps were based on average steric and electrostatic fields, resulting in PLS models with higher predictive power and r^2(cv) values of 0.584, 0.691, and finally 0.749, while conventional r^2 values of 0.830, 0.897, and 0.928 were obtained.

For alignment C1 resulting from flexible field fit using A1, a CoMFA model with an r^2(cv) value of 0.618 and a conventional r^2 of 0.879 resulted. After two rigid field fit realignment steps were applied, models with improved statistical properties with r^2(cv) values of 0.645 and 0.698 were found (conventional r^2: 0.897 and 0.916), while the energy minimization of alignment C3 (Figure 4) to C4 resulted in a model with a r^2(cv) of 0.574 and a conventional r^2 of 0.879.

As any approach to improve the internal consistency of PLS models by realignment might result in overfitting, more rigorous validation was applied to support the statistical quality and predictive power of all 12 QSAR models. For each model reported in Table S1 of the Supporting Information, 300 validation runs were analyzed as follows: 100 with randomized activities, 100 with two, and 100 with five randomly assigned cross-validation groups. First, biological activities were randomly assigned[64] to molecules and subjected to leave-one-out PLS analysis. The mean r^2(cv) value for 100 randomizations is reported in Table S2 (Supporting Information) in columns Rand100 and SD(Rand100). All models show mean r^2(cv) values lower than −0.130; no model was obtained with more than two PLS components, thus supporting the finding that PLS models from Table S1 are significantly better than random models based on the same alignment.

Progressive scrambling[65] was applied to test PLS model stability against small perturbations of the *y*-block. After biological activities were subdivided into 2−12 subgroups, these activities within a subgroup were randomized, while the relationship between subgroups remained unaffected. Using 12 subgroups only, a small perturbation was probed, while for two subgroups, a much larger portion of the *y*-block was randomized. The progressive scrambling results were given in the Supporting Information, while the mean cross-validated r^2 averaged over 20 individual randomizations per alignment and the subgroup was plotted vs the number of subgroups per alignment in Figure 5. With only one subgroup, the results were similar to randomization; negative r^2(cv) values are observed. The increase of the mean r^2(cv) with more subgroups is obvious from Figure 5A−C.

In general, r^2(cv) values for alignment A1 are lower than for A2−A4, showing that rigid field fit increases the consistency of the data set. Interestingly, a subdivision into three subgroups produced stable PLS models and reasonable mean r^2(cv) values for all 12 alignments. For alignments B and C (Figure 5B,C), the mean r^2(cv) per subgroup does not correlate to rigid fitting alignment order, while no model after realignment has a decreased error tolerance as an indicator of overfitting.

The interpretation of related plots aids in understanding the effect of biological errors on PLS predictions and provides an estimate of model stability. If any alignment led to overfitting of biological data regardless of acceptable leave-one-out r^2(cv) values, this becomes obvious; as increased perturbations in biological data should have a dramatic effect on the mean r^2(cv) values, any correlation should disappear. Hence, plotting of mean r^2(cv) values for increased perturbation over related

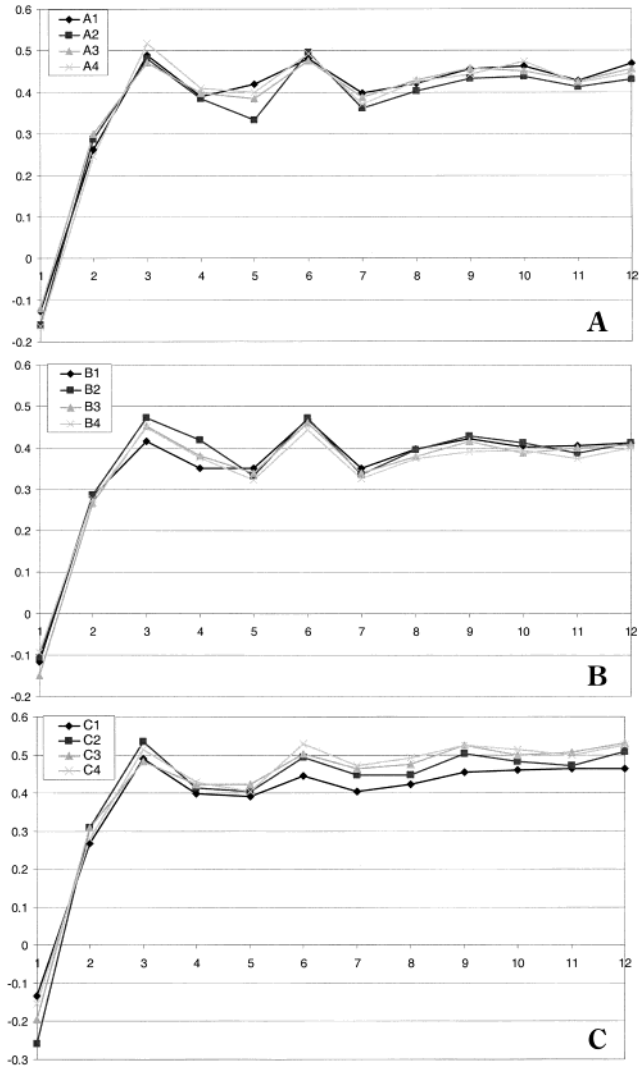

Figure 5. Results from progressive scrambling for PLS models from different alignments. The mean r^2(cv), averaged over 20 randomizations per alignment, is plotted vs the number of subgroups: (A) alignments A1−4, (B) alignments B1−4, and (C) alignments C1−4.

alignments shows that derived models do not become more dependent on the biological data. Thus, the applied iterative realignment procedure does not artificially increase the internal data set consistency by overfitting, while decreasing the error tolerance.

Although cross-validation estimates the predictive power of a PLS model, leave-one-out produces over-optimistic r^2(cv) values. Hence, additional PLS analyses were done using two and five randomly chosen cross-validation groups. Because of random formation of cross-validation groups, each analysis for a particular alignment was repeated 100 times, and statistical results are reported in Table S2 in columns q2(2CV), SD(2CV) for two and q2(5CV), SD(5CV) for five cross-validation groups. All derived mean r^2(cv) values count for stable and significant PLS models for each alignment. Two cross-validation groups produce a lower r^2(cv) value, as a larger portion of each data set (50%) is assigned to a test group each time for prediction of activity. From the distribution of 100 individual r^2(cv) values per model, it is obvious that some analyses with low r^2(cv) values are indicating some inconsistency in these data set and alignment. However, each realignment step consistently produced increased averaged r^2(cv) values and lower standard deviations, thus revealing that statistical significance and model predictivity could be improved using this realignment strategy. In general, the cross-validated r^2(cv) values using five groups were only slightly lower than those obtained using the leave-one-out method, and they also show a low standard deviation. From inspecting those parameters, the model C3 was chosen for chemical interpretation, as it was stable and reliable for further design.

3.3. 3D-QSAR Analysis Using CoMSIA. As the realignment was based on CoMFA, CoMSIA as an alternative descriptor was evaluated. CoMSIA statistical results based on alignments A−C are summarized in Table S3 (Supporting Information) using only steric and electrostatic similarity index fields (SE, upper part of Table S3) or steric, electrostatic, and hydrophobic fields (SEH, lower part of Table S3). The addition of the hydrophobic field led to improved r^2(cv) values; for all 12 models, four component models were obtained. For the atom-based alignment A1, a CoMSIA model with an r^2(cv) value of 0.449 for four relevant PLS components and a conventional r^2 of 0.765 was obtained, in the same range than obtained for CoMFA, while improved as compared to the steric and electrostatic CoMSIA analysis. However, the internal consistency of this model was only slightly improved after realignment, which is in agreement with a lower dependency of CoMSIA fields to cutoff effects. For alignments A2−4, r^2(cv) values of 0.429, 0.443, and 0.453 were observed, while all models lead to similar chemical interpretation. The hydrophobic field contributes 40−48% to these models, while the electrostatic and steric fields show a 30−41 and 19−22% contribution, respectively, suggesting that CoMFA steric fields are a careful balance between steric and hydrophobic effects.

For alignment B1, a CoMSIA model with an r^2(cv) value of 0.479 for four PLS components and a conventional r^2 of 0.774 was obtained. The realignment produces r^2(cv) values of 0.499, 0.560, and 0.641 for B2−4, respectively, while conventional r^2 values of 0.787, 0.820, and 0.865 were found. Finally, alignment C1 led to a model with an r^2(cv) value of 0.536 and a conventional r^2 of 0.801, while after realignment r^2(cv) values of 0.547, 0.549, and 0.543 for C2−4 were obtained.

For model validation of all alignments, similar approaches than those described for CoMFA were applied to the CoMSIA models based on steric, electrostatic, and hydrophobic fields; all results are summarized in Table S4 (Supporting Information). Repeated randomizations of biological activities led to mean r^2(cv) values lower than −0.120 for all models, thus demonstrating the significance of all models.

Additional PLS analyses were run 100 times for each alignment using two and five randomly chosen cross-validation groups. Statistical results are reported in Table S4 in columns q2(2CV), SD(2CV) for two and q2(5CV), SD(5CV) for five cross-validation groups. As for CoMFA, all derived mean r^2(cv) values count for stable and significant PLS models. Again, B4 is the best CoMSIA model, while only for alignment B, the realignment produces increased r^2(cv) values and lower standard deviations after averaging over r^2(cv) values,

showing that this procedure led to improved significance and predictivity.

3.4. 3D-QSAR Model Validation Approaches. The final 3D-QSAR models were subjected to further validation to evaluate their predictivity and stability with respect to parametrization, different probe atoms for computing molecular fields, and influence of ligand alignment perturbations and conformational energies. First, the influence of increasing information in *X*-space on predictivity of the final CoMFA and CoMSIA models was assessed.[68] The chosen approach is based on progressively dividing the set of compounds into training and test sets using statistical design toward a rigorous evaluation of the QSAR models' external prediction capabilities. Representative training sets with increasing populations of 20−62 molecules in increments of two compounds were selected using a maximum dissimilarity algorithm[69,70] and 2D fingerprints, as described earlier.[68] For each subset, a leave-one-out PLS analysis served to extract the r^2(cv) for the optimal number of components, followed by a PLS analysis without cross-validation. This noncross-validated model is applied for predicting the test set, resulting in a predictive r^2 value for each submodel. The dependency of this predictive r^2 value vs the population and diversity of each submodel can be used to evaluate its predictivity toward external prediction sets. This approach also allows to estimate a confidence interval for reliable prediction in terms of structural similarity of novel candidates to the training data set, for which an affinity prediction is expected reliable guidelines for a chemical optimization program.

The r^2 values for both CoMFA and CoMSIA models C3 are plotted in Figure 6 vs the number of compounds in each training set. For CoMFA, the r^2(cv) value is low with less than 40 compounds in the training set (Figure 6A). Although the conventional r^2 is high, the predictivity is not sufficient. The mean Tanimoto coefficient for this training set is 0.76, while the most similar compounds show a Tanimoto coefficient of 0.85. For 40 compounds in the training set, a predictive model with a cross-validated r^2 of 0.483 and a predictive r^2 of 0.661 results.

When increasing the subset size to more than 46 compounds, the cross-validated r^2 reaches values between 0.55 and 0.68. Correspondingly, predictive r^2 values larger than 0.67 are obtained, which indicate stable PLS models with good predictive capabilities. This demonstrates that a reliable affinity prediction can be expected for candidates with a larger similarity than this maximum Tanimoto threshold of ∼0.85. The degree of extrapolation increases with decreasing similarity, then causing less reliable predictions.

For CoMSIA, this analysis produces similar results: PLS models with more than 48 compounds in the training data set lead to significant cross-validated r^2 values between 0.4 and 0.55, while predictive r^2 values between 0.69 and 0.84 are obtained with one exception (Figure 6B), counting for significant and stable CoMSIA models, which allow one to predict biological activities for structurally similar candidates.

A more rigorous model validation for 3D-QSAR is the prediction of an external set. As no additional active compounds were available at the time of this study, the entire data set was split into a training and test data set by selecting 50 training compounds using statistical design techniques as described above. The test set encompasses 15 compounds from Table 1: **007**, **027**, **028**, **149**, **185**, **225**, **261**, **301**, **306**, **310**, **313**, **317**, **329**, **330**, and **333**. From the previous studies, it is assumed that the remaining training set captures the chemical diversity of the investigated inhibitors. Subsequently, 3D-QSAR models using CoMFA and CoMSIA were derived, statistically validated, and employed for prioritization of 15 candidates in the test set. Using a 2 Å grid spacing, a CoMFA model with an r^2(cv) value of 0.615 for four relevant PLS components and a conventional r^2 of 0.920 were obtained. The contribution of steric and electrostatic field descriptors to the overall variance and the chemical interpretation of the model in terms of 3D contour visualization and interpretation is very similar to the full CoMFA model C3 reported above. Similar agreement is observed for the corresponding CoMSIA model with 50 compounds, 2 Å grid spacing, an r^2(cv) value of 0.436 for three relevant PLS components, and a conventional r^2 of 0.841. To be consistent with the original CoMFA and CoMSIA models, a full validation of both training set models was carried out. The randomization of biological activities led to mean r^2(cv) value for 100 runs of −0.185 for CoMFA (SD, 0.148) and −0.202 for CoMSIA (SD, 0.180), indicating that both PLS models are significantly better

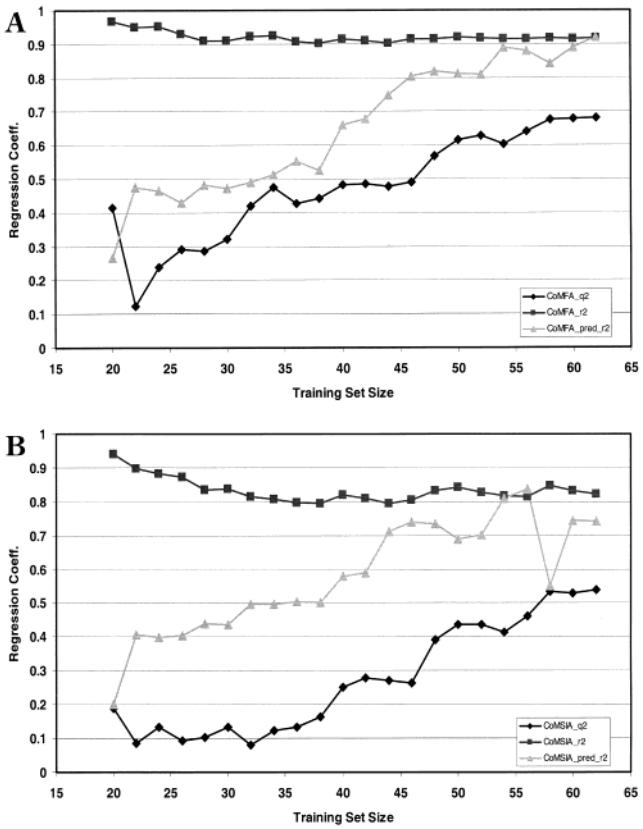

Figure 6. Validation and predictivity assessment of NOS-I 3D-QSAR models. Several smaller training sets were designed using maximum dissimilarity methods. Comparison of cross-validated, conventional, and predictive r^2 values for individual PLS models for a particular training set on the *y*-axis vs training set size using (A) CoMFA or (B) CoMSIA as descriptor for PLS.

than random models based on the same alignment. Similar results were obtained after progressive scrambling[65] to test both PLS models' stability against small perturbations in the *y*-block (no data given). Additionally, 100 PLS analyses using two and five randomly chosen cross-validation groups were done, resulting in mean r^2(cv) values of 0.385 (two cross-validation groups; SD, 0.124) and 0.545 (five cross-validation groups; SD, 0.050) for CoMFA and 0.266 (two cross-validation groups; SD, 0.109) and 0.370 (five cross-validation groups; SD, 0.067) for CoMSIA, respectively. These derived mean r^2(cv) values count for stable and significant PLS models, which then were used for prediction of the external test set. Subsequent predictions for all 15 test set compounds resulted in high predictive r^2 values of 0.812 for CoMFA and 0.688 for CoMSIA. The corresponding predictive r^2 value for CoMSIA is found to be only slightly lower than observed for CoMFA. Hence, this use of a designed test set provides a definitive evaluation of the high predictivity of both final 3D-QSAR models used for chemical interpretation.

In addition, the quality of both CoMFA and CoMSIA models was assessed with respect to force field parametrizations, the ligand conformation, and alignment perturbations around the best alignment-based PLS models. The effect of compound alignment relative to the grid position within the predefined region definition file was evaluated by consistently moving all compounds of the final PLS model C3 in increments of 0.5 Å in all three dimensions *x*, *y*, and *z*. In this study, the relative alignment is not changed, but the absolute orientation with respect to the grid is changed. The obtained r^2(cv) values for each orientation based on CoMFA descriptors range from 0.568 to 0.698 (mean r^2(cv), 0.622; SD, 0.04) for four component PLS models, suggesting only a minor dependence of the final model on the absolute orientation of the grid box. No dependency of the relative alignment to the grid is found for CoMSIA, as expected.[40,71] The effect of different choices of the origin of the grid for CoMFA was investigated using 15 atom types in addition to carbon C3 as probe atoms with a 2 Å grid spacing. The r^2(cv) values for each probe atom range from 0.674 to 0.698 for four components PLS models with C3 and other carbon-based atom types showing the highest r^2(cv) values, showing only a slight dependence on the chosen probe (mean r^2(cv), 0.682; SD, 0.01).

To evaluate the dependency of the final models from the relative alignment and chosen conformer for PLS, the following approach was applied. First, the influence of alignment differences on the predictive ability of the models was evaluated by systematically translating one molecule at a time in *x*, *y*, or *z* directions in 10 steps between −0.5 and 0.5 Å. Each molecule was subjected once to this study. Each new orientation was used for prediction of biological activity from (i) the original CoMFA model and (ii) a new CoMFA model excluding this particular molecule toward a leave-one-out cross-validation procedure. All predictions were compared to experimental activities, the predicted activity variations plus residuals were averaged to provide a measure of how perturbations in the relative alignment affect the predictive power of the PLS models (Table S5, Supporting Information). The entry Translation in Table S5 summarizes these data for predictions with the original CoMFA model, while Translation CV refers to predictions based on the cross-validation approach.

Similar studies were undertaken with systematically generated conformations for each molecule at a time. The program FlexS[72] was used to automatically superimpose each candidate molecule onto the most similar compound in the remaining data set, and the top 30 superposition solutions resembling the general shape and key interactions were analyzed. Each of these conformations was used for affinity predictions using the original model (entry FlexS in Table S5) and the cross-validation strategy with a PLS submodel excluding this molecule (FlexS CV in Table S5). In addition, the FlexS-generated conformations were (i) minimized prior to prediction (FlexS EM and FlexS EM CV in Table S5) or (ii) minimized and matched to the common bicyclic core using rms fitting (FlexS EM Match and FlexS EM Match CV in Table S5). The averaged residuals for compound translation with and without cross-validation are lower (0.143 without and 0.221 with cross-validation) than those derived from different conformers generated using the different protocols (0.267−0.332), while those values are comparable to the standard deviations of the original CoMFA models (Table S1, 0.291−0.378 for models A1 to C4). These data provide clear insight into the stability of the CoMFA models with respect to the alignment and conformation. While minor perturbations clearly influence affinity predictions, this is within the error for the derived cross-validated PLS models, thus supporting stable models with respect to parametrization and underlying assumptions.

To assess the influence of conformational energy upon building the alignment prior to PLS statistical analysis, each compound from model C3 was extensively minimized. The conformational energy differences per compound were included into additional PLS models, namely, the total energy plus individual force field terms (bond stretching, angle bending, torsional, van der Waals, and electrostatic energy terms[44,43]). A mean value of 17.5 kcal/mol for the total energy difference was computed (SD, 19.2), while for individual terms mean values were obtained as follows: bond stretching, 1.24 (SD, 2.08); angle bending, 5.06 (8.05); torsional, 2.42 (5.62); van der Waals, 5.71 (7.70); and electrostatic energy, −0.01 (0.80). However, no energy term alone, in combination with CoMFA descriptors or CoMFA plus energy-derived descriptor terms led to models with improved predictivity (no data given). In addition, 30 molecular descriptors including surface-derived terms, functional group counts, PM3 ionization potential, and electron affinity, globularity, polarizability, free energy of solvation in different solvents (water, octanol, hexadecane), octanol/water partition coefficient, and solubility were computed using the program QikProp,[73] while again, none of these terms could significantly improve the final CoMFA model, when using it in combination with CoMFA fields (no data given). All validation studies clearly demonstrate the predictive power of the final CoMFA model and its stability with respect to factors including parametrization, ligand conformation, strain energy, and absolute alignment of individual molecules.

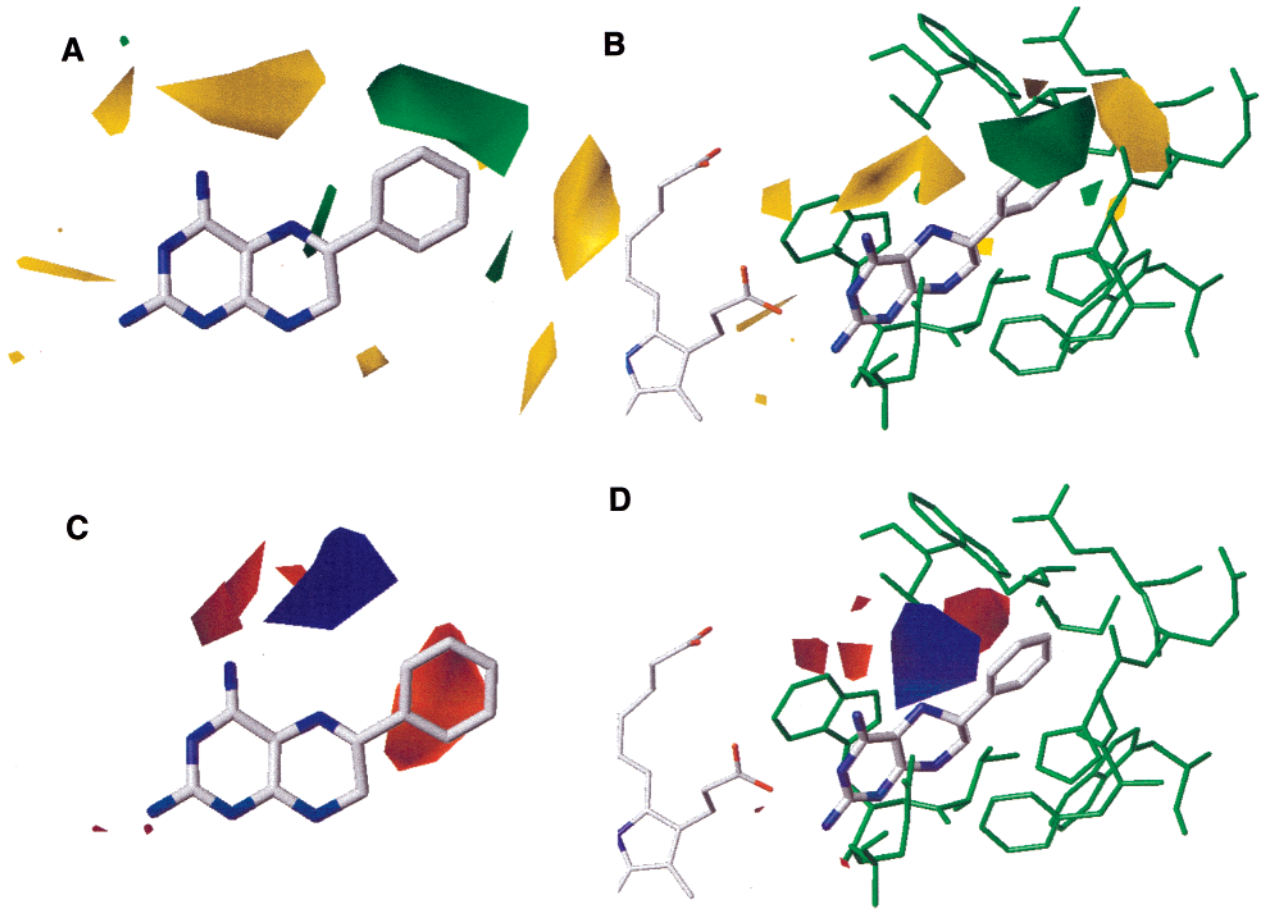

Figure 7. Contour maps for CoMFA analysis C3 in combination with the inhibitor 185 (IC_{50} 6 μM). (A) Steric SD*Coeff contour map: green contours (>85% contribution) indicate sterically favored regions, and yellow contours (<15% contribution) indicate disfavored areas. (B) Same as A with NOS-I binding site. (C) Electrostatic SD*Coeff contour map: blue contours (>85% contribution) refer to regions where negatively charged substituents are disfavorable, and red contours (<15% contribution) indicate regions where negatively charged substituents are favorable. (D) Same as C with NOS-I binding site.

3.5. Chemical Interpretation of the QSAR Models and Comparison to Protein Topology. On the basis of alignment consistency and validation for CoMFA and CoMSIA, the PLS analysis C3 was selected for discussion, while analyses A4 and B4 both led to similar chemical interpretation. The steric and electrostatic SD*Coeff CoMFA fields from analysis C3 are displayed as contour maps in Figure 7 with the potent inhibitor **185** having a phenyl substituent attached at C6 to the 4-amino-5,6,7,8-tetrahydropteridine scaffold (IC_{50} = 6 μM). Corresponding plots for models A4 and B4 are given in the Supporting Information, respectively. For Figure 7B,D, selected binding site residues from the NOS-I homology model are shown in addition. On the upper panel, the steric field contributions correlated with biological activity are shown. Green contours (>85% contribution) indicate those regions where steric bulk is favorable for new inhibitors, while yellow contours (<15% contribution) highlight regions that are detrimental for biological activity. A similar analysis is done for the electrostatic SD*Coeff field (Figure 7, lower panel). Blue contours (>85% contribution) refer to regions in space where an increase of positive charge (or a decrease of negative charge) is favored for new ligands to enhance potency, while red contours (<15% contribution) indicate those regions where an increase of negative charge is favorable for higher biological activity. Although 3D-QSAR results were derived taking only ligand information into account, the PLS contour maps are discussed with the binding site topology from the NOS-I model to show consistency with steric, electrostatic, and hydrophobic requirements.

Consistently, one large sterically favorable region is present in agreement with requirements of the pterin-binding site. One green contour region at the phenyl ring attached to C6 is pointing to a pocket formed by residues from the first and second NOS dimer: Val(Met)106, TrpB076, TrpB447, HisB463, and GluB465. The NOS-III residue numbering is used for the following discussion; differences for NOS-I are indicated in brackets. This subsite is not occupied by any ligand atom in the **32**/NOS-III complex, while CoMFA points out the importance of this region to achieve ligand complementarity for reasonable binding affinities. Several bulky, hydrophobic substituents attached to C6 of the central scaffold improve binding affinity. The inspection of, for example, the 4-oxo series (Table 1a) reveals a clear correlation of steric bulk with binding, exemplified by inhibitors **342** (thiophene, 29 μM), **261** (phenyl, 26 μM), and **341** (naphthyl, 8 μM). In the natural substrate H_4-Bip, this pocket is occupied by the dihydroxypropyl chain. Especially, the visual inspection of PLS models B4 (Supporting Information) and C3 (Figure 8) indicates

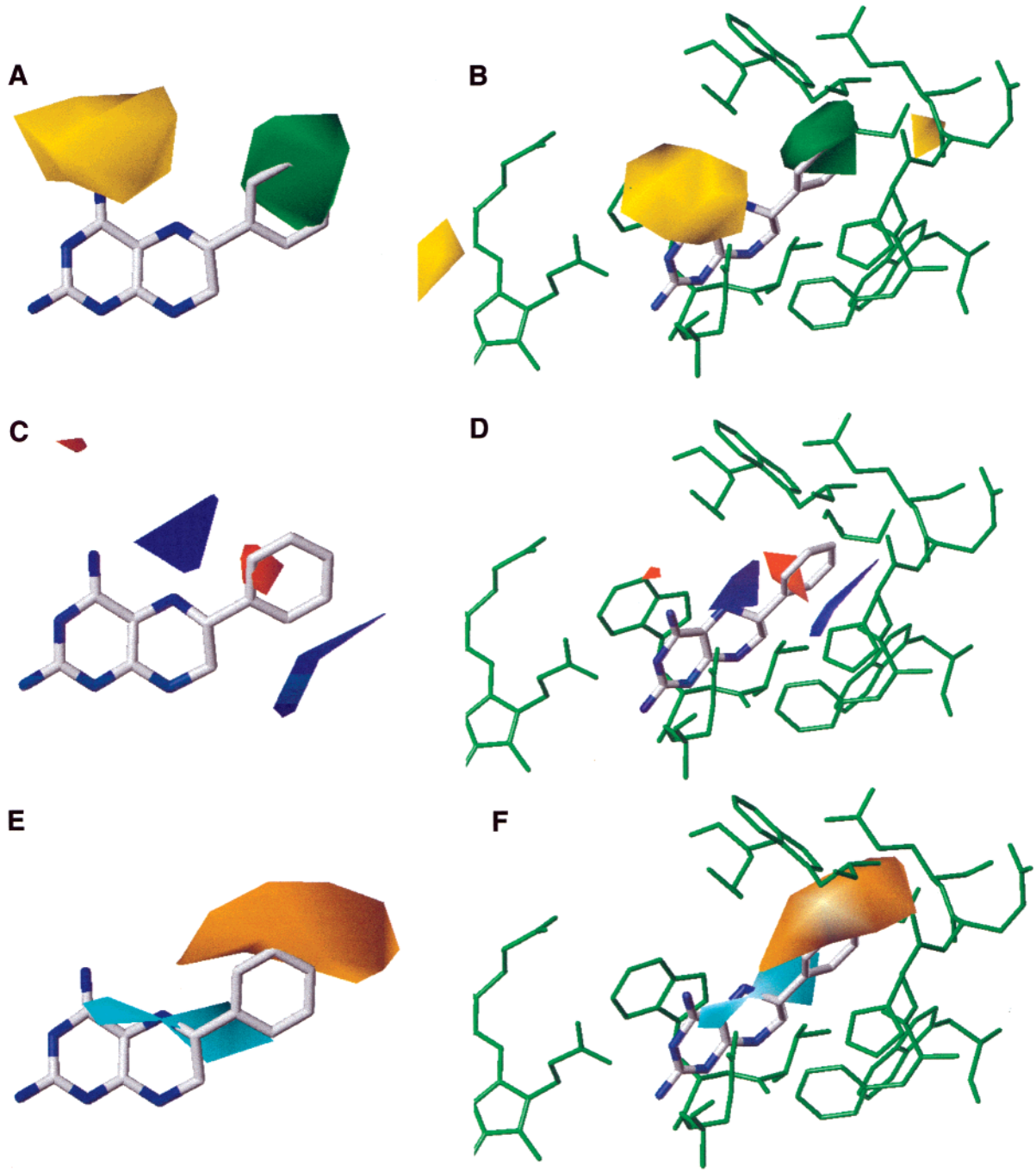

Figure 8. Contour maps from CoMSIA analyses for model C3 in combination with inhibitor **185** (IC_{50} 6 μM). (A) Steric SD*Coeff contour map: green contours (>85% contribution) refer to sterically favored regions, and yellow contours (<15% contribution) indicate disfavored areas. (B) Same as A with NOS-I binding site. (C) Electrostatic SD*Coeff contour map: blue contours (>85% contribution) refer to regions where negatively charged substituents are disfavorable, and red contours (<15% contribution) indicate regions where negatively charged substituents are favorable. (D) Same as C with NOS-I binding site. (E) Hydrophobic SD*Coeff contour map: cyan contours (>85% contribution) refer to regions where hydrophilic substituents are favorable, and orange contours (<15% contribution) indicate regions where hydrophobic substituents are favorable. (F) Same as E with NOS-I binding site.

not only the favorable but also the detailed unfavorable interactions indicating the size of this subsite. Similar information is present in all models at lower contour levels. Val106 is replaced by Met in NOS-I and NOS-II adopting a similar position in the NOS-II X-ray structure and the NOS-I homology model. When inspecting X-ray crystal structures of H_4Bip/NOS complexes,[7,8] it is obvious that the bulkier Val106 side chain makes a tighter contact with the pterin atom N5 than the corresponding Met residue. This region imposes different steric constraints on diverse inhibitors and thus provides possibilities to gain isoform selectivity. A small number of differing residues was sufficient in other examples to achieve isoform selectivities.[74]

A yellow contour close to the tetrahydropteridine C7 shows that bulky substitution affects activity in a negative way, which is in accord with NOS binding site constraints due to Ser104 and TrpB447. Although a

phenyl ring at C7 is tolerated, it reduces activity, when comparing inhibitors **185** and **186**. However, larger substituents are not tolerated.

Yellow contours left of the 2-amino group and N3 reveal that an unsubstituted 2-amino group has optimal steric requirements to interact with the NOS protein binding pocket including the heme carboxylates. As the 5,6,7,8-tetrahydropteridine is hydrogen-bonded to one heme carboxylate by direct interactions and via structurally conserved water, bulky substitution in this region will significantly affect the ability to undergo this interaction. The yellow contour close to N3 is directly superimposed with one of the heme carboxylates. The 2-amino group interacts via solvent with the heme carboxylate and the backbone carbonyl of Trp449. These contours further indicate that replacement of any structural water from the hydrogen bond interactions will decrease biological affinity.

Another unfavorable region is located close to the tetrahydropteridine C4 substituent due to constraints from the Arg367 side chain plus the narrow entrance into this binding site. Arg367 is conserved in all NOS isoforms. In the **185** X-ray structure, the guanidine is directed toward the inhibitor 4-amino group, although not providing an optimal interaction geometry. In contrast, the **32** carbonyl oxygen is interacting with this side chain. Only those 4-amino substituents are tolerated, which optimally fill the narrow entrance into the H_4Bip binding site by one or two benzylic groups (**303**, **305**, and **306**). This H_4Bip entrance region is occupied by a glycerol molecule in the NOS-III structure, while it might be replaced by solvent in the absence of glycerol.[8] When substituting the 4-amino group by a piperidine or morpholine ring (compounds **311**, **313**, **315**, and **317**), the biological activity decreases significantly, as more steric bulk is located at the narrow H_4-Bip site entrance. However, the potent 4-amino inhibitors with bulky dibenzyl substitutions at N4 (Table 1f, **303**, **305**, and **306**) are in agreement with CoMFA steric field results, as two smaller green contours above the yellow contour at N4 and below N5 point to favorable steric interactions with the protein, while it is obvious that the interaction at both favorable regions along with filling additional space between Met106, TrpB076, and Trp449 resulted in increased binding affinity, e.g., for the lipophilic inhibitor **306** (2 μM) as compared to **246** with a less demanding N4 dimethyl substitution (75 μM) and **311** with a morpholine (82 μM).

Inspection of CoMSIA steric SD*Coeff contour maps (Figure 8) for the same model C3 shows a high correspondence to CoMFA, although the steric field explains only 21% of the overall variance. The electrostatic field accounts for 30% of the overall variance, while the main part of 49% is due to hydrophobic interactions, which are only included in CoMSIA. For all other CoMSIA models, those contributions are similar. One advantage of CoMSIA is that entropic contributions, which cannot be completely treated using Lennard−Jones and Coulombic fields, are modeled using hydrophobic similarity index fields. The steric SD*Coeff contour maps point to favorable ligand regions (green >85% contribution), indicating size and shape of substituents binding into the H_4Bip dihydroxypropyl subsite. Sterically unfavorable regions at C4, the 2-amino group, and the region at C7 are indicated by yellow contours (<15% contribution). These contours are compact and centered on the ligand atoms, while CoMFA regions highlight complementary features of the receptor site.

The electrostatic SD*Coeff contour maps are also in agreement for CoMFA (Figure 7) and CoMSIA (Figure 8) for individual alignments, while small differences for different alignments are present. Blue contours (>85% contribution) represent regions where more positive charge or a reduction of negative charge is favorable to enhance biological potency, while red contours (<15% contribution) indicate regions where more negative charge is favored. One blue contour region is located in the binding site entrance region above N5, suggesting that more positive electrostatic potential in this region enhances ligand binding. The side chains of Val(Met)-106 and Arg367 are directed toward this entrance, while the latter guanidine is found to undergo a water-mediated interaction with N5 in X-ray structures of related isoforms. This region explains affinity differences between the reduced and the aromatic scaffold, e.g., for 4-oxo, 6-phenyl derivatives **187** (reduced 7.3 μM) and **261** (aromatic 26 μM). For a detailed comparison of both similar molecules, their surrounding electrostatic field is shown in Figure S4 (Supporting Information), revealing that positive charge above N5 for the water-mediated interaction is only present in **187** (left).

A second blue contour is located in the region close to C7, pointing toward the face of the aromatic ring of PheB462. A red contour region is located in the H_4Bip dihydroxypropyl binding pocket close to C6, suggesting that electron-rich aromatic systems are favored in this pocket. Another red contour is located above the C4 substituents at the binding site entrance, suggesting the favorable effect of increased negative charge in this region, mainly to establish a water-mediated hydrogen bond to one of the heme propionates.

To estimate entropic contributions to ligand binding, hydrophobic similarity index fields were analyzed. Regions with favorable hydrophilicity are indicated by cyan contours in Figure 8E (>85% contribution) centered at C4, N5, and C6 of the 5,6,7,8-tetrahydropteridine. In contrast, the pocket accommodating the C6 phenyl substituent is filled by an orange region (<15% contribution), showing an area for preferred hydrophobic interactions, which agrees to the amino acid properties forming this part of the H_4Bip binding site. Hence, increasing polarity at the scaffold, while increasing hydrophobic interactions in this subpocket, has a positive effect on inhibitor binding.

Inspecting all contour regions from model C3 (and A4 and B4, Supporting Information), the ligand binding modes from literature X-ray data could be confirmed. Hence, the binding mode of all other than the two reference compounds **185** and **32** is validated using 3D-QSAR models; their complementarity to the receptor topology is obvious from inspection of Figure 7B,D for CoMFA and 7B,D,F for CoMSIA with detailed protein−ligand interaction requirements for the NOS-I binding site. In addition, CoMFA steric and electrostatic SD*Coeff contour maps are shown in combination with **185** and the Connolly surface generated using the NOS-I H_4Bip binding site. Some parts in the foreground were cut to

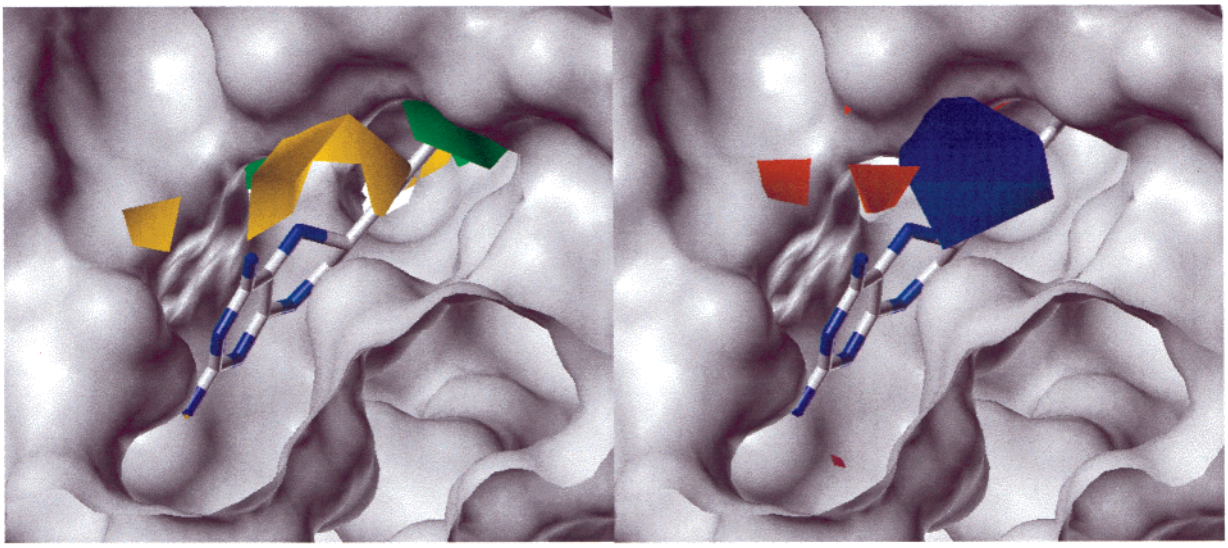

Figure 9. CoMFA contour maps for analysis C3 in combination with **185** and the NOS-I binding site Connolly surface. Some regions are cut to allow for a better view into the binding site cavity. (A) Steric SD*Coeff contour map. (B) Electrostatic SD*Coeff contour map. For details, see Figure 7.

allow for a better view into this cavity and show steric and electrostatic complementarity. Those figures reveal that favored regions show a good fit to the H_4Bip binding site, while a similar complementarity is observed for electrostatic and hydrophobic interactions. Hence, the analysis of 3D-QSAR results led to a clear and consistent picture in close agreement with the protein topology for the NOS-I homology model and the X-ray structure information for NOS-II and NOS-III, thus allowing for a design of novel NOS-I inhibitors combined with accurate affinity predictions (Figure 9).

3.6. NOS-I Inhibitor Isoform Selectivity. The design of isoform selective NOS inhibitors requires a combined interpretation of X-ray structures with emphasis on differing binding site residues and a series of inhibitors with modulated chemical functionalities. The structural comparison of experimental and modeled H_4Bip binding sites for NOS isoforms reveals two major differences, namely, the replacement of NOS-III Val106 against Met for NOS-II and NOS-I and Ala148 in NOS-III replaced by Ile or Val in NOS-II and NOS-I, respectively. Both alterations offer the design of selective ligands toward only one isoform using the scaffolds summarized in Table 1. Testing the most active NOS-I inhibitors against other NOS isoforms revealed some remarkably selective inhibitors toward NOS-I. One of the most selective compounds from the 4-oxo series is **183** (Table 1a) with IC_{50} values of 44.0, 374.2, and 208.6 μM for NOS-I/II/III, respectively. For the 4-amino series, substitutions at N4 in combination with aromatic substituents at C6 both directed toward the binding site region encompassing the Val106 side chain reveal a favorable selectivity profile for NOS-I, as exemplified by compound **334** (Table 1j) with 5.0 μM as compared to 214.2 and 31.7 μM for NOS-II and NOS-III, respectively. Those compounds have appropriate substitutions at the pteridine 4- and 6-positions directed toward Val106 in NOS-I. This valine side chain is bulkier than Met and involved in contact with preferrably hydrophobic substituents at the pteridine 4- or 5-positions in NOS-II and NOS-III. Its decreased flexibility could also positively affect protein−ligand interactions.

Thus, this region imposes steric constraints in combination with hydrophobic interactions and might lead to selectivity by adding certain substituents at the N5 and C6 positions of the pteridine scaffold as well as substituting N4 in the 4-amino series. Further details including isoform SAR data and interpretation in structural terms will be given elsewhere.

4. Conclusion

The present study was focused on developing and validating predictive 3D-QSAR models for 65 inhibitors of human neuronal NOS (NOS-I). Different alignment rules have been used and refined using iterative realignment. An improvement of the statistical quality of the resulting models was achieved by a rigid field fit to minimize steric and electrostatic field differences of molecules to the corresponding average field. This procedure was able to increase the internal consistency and predictivity of all 3D-QSAR models, as it was shown by application of validation studies for each resulting model. Finally, one model was selected from each series for chemical interpretation leading to similar results. Those best models allow us to use a consensus model prediction strategy for designing novel NOS-I inhibitors. The preferred model C3 was selected by analysis of 3D-QSAR validation results, especially from various cross-validation strategies and progressive scrambling. The chemical interpretation of this model in terms of inspecting the steric and electrostatic contour maps reveals a good correspondence to topological features of the NOS−H_4Bip binding site. Thus, a detailed picture of requirements for NOS-I inhibition emerges from this study, combining 3D-QSAR, X-ray structure data, and homology modeling toward a better understanding of protein−ligand interactions.

5. Experimental Section

5.1. Chemistry. Thin-layer chromatography (TLC): precoated silica gel thin-layer sheets F 1500 LS 254 and precoated cellulose sheets F1440LS 254 were from Schleicher and Schüll. Flash chromatography (FC): silica gel (Baker, 30−60 μm),

0.3−0.4 bar. UV/vis: Perkin-Elmer, Lambda 15; λ_{max} in nm (log ϵ). ^{1}H nuclear magnetic resonance (NMR): Bruker AC-250 and WM-250; δ (ppm) relative to dimethyl sulfoxide (DMSO)-d_6.

The synthesis of compounds **159**, **179**, **183**, and **215** is described in ref 75; the synthesis of **200** and **201** is described in ref 76; the synthesis of **199** is described in ref 77; and the synthesis of other compounds not described here is given in refs 35 and 36.

5-(4-Azidobenzoyl)-6-(4-azidobenzoyloxymethyl)-5,6,7,8-tetrahydropterin (150). A suspension of 6-hydroxymethyl-5,6,7,8-tetrahydropterin[36] (0.2 g, 0.74 mmol) in dry pyridine (10 mL) was treated under N_2 atmosphere with 4,4′-azidobenzoic anhydride (0.92 g, 3 mmol) with stirring at room temperature for 28 h. The reaction solution was evaporated to dryness and coevaporated three times with toluene, and then, the residue was treated with MeOH in an ultrasound bath. The solid was filtered off, washed with MeOH and ether, and dried in high vacuum at 40 °C to give 0.183 g (51%) of yellowish powder; mp >295 °C (dec). UV (MeOH): 212 (4.70), 271 (4.64), 328 (3.95). ^{1}H NMR (DMSO-d_6): 9.74 (bs, 1 H, H−N(3)); 8.00 (d, 2 H, ph); 7.48 (d, 2 H, ph); 7.25 (d, 2 H, ph); 7.01 (d, 3 H, ph, H−N(8)); 6.17 (bs, 2 H, NH_2); 5.00 (bs, 1 H, H−C(6)); 4.20 (m, 2 H, CH_2O); 3.52 (m, 2 H, H−C(7)). Anal. ($C_{21}H_{17}N_{11}O_4 \times 0.5H_2O$) C, H, N.

N^2-Methyl-5,6,7,8-tetrahydropterin Dihydrochloride (189). N^2-methylpterin (0.531 g, 3 mmol) was dissolved in trifluoroacetic acid (25 mL), the PtO_2 (0.1 g) was added as a catalyst, and the mixture was reduced under hydrogen atmosphere in a shaking apparatus for 12 h. The catalyst was filtered off, and the filtrate was evaporated to dryness. The residue was treated with methanolic HCl (12%, 20 mL) under stirring. The resulting precipitate was collected, washed, with MeOH, and dried in a vacuum desiccator over KOH to give 0.55 g (84%) of a colorless crystal powder; mp 248−250 °C. UV (pH 0): 266 (4.13). Anal. ($C_7H_{11}N_5O \times 2HCl \times H_2O$) C, H, N.

2-Amino-4-*n*-pentyloxy-6-[(2-phenyl)-1,2-dibromoethenyl]pteridine (265). A solution of 2-amino-4-*n*-pentyloxy-6-phenylethinylpteridine[36] (0.1 g, 0.3 mmol) in $CHCl_3$ (3 mL) was heated to 40 °C. Then, a solution of bromine in $CHCl_3$ (1%, 0.3 mL) was added dropwise. After it was stirred for 3 h, the solution was evaporated, and the residue was dissolved in a small amount of $CHCl_3$ and purified by silica gel chromatography with $CHCl_3$. The main fraction was evaporated, and the resulting syrup was crystallized from *n*-hexane (3 mL)/$CHCl_3$ (2 mL) to give 0.1 g (68%) of yellow needles; mp 182−183 °C. Anal. ($C_{19}H_{10}Br_2N_5O$) C, H, N.

2-Amino-4-*n*-pentyloxy-6-phenacetylthiopteridine (270). To a solution of 2-amino-4-*n*-pentyloxy-6(5H)pteridinethione[78] (0.1 g, 0.38 mmol) in $CHCl_3$ (20 mL), triethylamine (60 mL) and phenacetylbromide (76 mg) in $CHCl_3$ (10 mL) were added. The solution was stirred for 3.5 h at room temperature and evaporated. The residue was dissolved in a small amount of $CHCl_3$ and purified on a preparative silica gel plate (40 cm × 200.2 cm) with $CHCl_3$/MeOH (4:1). The main band was cut out, eluted, and evaporated, and the solid was recrystallized from EtOH (10 mL) to give 90 mg (63%) of yellow crystals; mp 190−192 °C. UV (MeOH): 244 (4.44), 285 (4.34), 397 (3.88). ^{1}H NMR ($CDCl_3$): 8.72 (s, 1 H, H−C(7)); 8.10 (m, 2 H, ph); 7.55 (m, 3 H, ph); 5.28 (bs, 2 H, NH_2); 4.76 (s, 2 H, CH_2S); 4.35 (t, 2 H, OCH_2); 1.62 (m, 2 H, CH_2); 1.30 (m, 4 H, CH_2-CH_2); 0.87 (t, 3 H, CH_3). Anal. ($C_{19}H_{21}N_5O_2S$) C, H, N.

2-Amino-4-dibenzylamino-6-(3,4-dimethoxyphenyl)-pteridine (306). A solution of 3,4-dimethoxyphenylglyoxalmonoxime (0.42 g, 2.84 mmol) in MeOH (10 mL) was added dropwise to a boiling solution of 2,5,6-triamino-4-dibenzylaminopyrimidine dihydrochloride[35] (0.78 g, 1.9 mmol) in MeOH (15 mL) and then heated under reflux for 3 h. After the solution was cooled, concentrated NH_3 was added to pH 9−10 and the resulting precipitate was collected, washed with H_2O, and dried. Recrystallization from DMF/H_2O gave 0.60 g (65%) of a yellow crystal powder; mp 200−201 °C. UV (MeOH): 209 (4.63), 253 (4.07), 295 (4.40), 315 (4.31), 409 (4.09). Anal. ($C_{28}H_{26}N_6O_2 \times 0.5H_2O$) C, H, N.

2-Amino-4-piperidino-6-(3,4-dimethoxyphenyl)pteridine (318). A solution of 3,4-dimethoxyphenylglyoxalmonoxime (1.78 g, 8.5 mmol) in MeOH (20 mL) was added dropwise to a boiling solution of 2,5,6-triamino-4-piperidinopyrimidine dihydrochloride[35] (1.6 g, 5.7 mmol) in MeOH (30 mL) and heated under reflux for 3 h. After the solution was cooled, concentrated NH_3 was added to pH 9−10, and the resulting precipitate was collected, washed with H_2O, and dried. Recrystallization from DMF/H_2O gave 1.25 g (56%) of a yellow crystal powder; mp 238−241 °C. UV (MeOH): 215 (4.57), 241 (4.27), 295 (4.44), 320 (4.13), 400 (4.04). Anal. ($C_{19}H_{22}N_6O_2 \times 1.5H_2O$) C, H, N.

2-Amino-6-(4-chlorophenyl)-4-piperidino-5,6,7,8-tetrahydropteridine (328). A solution of 2-amino-6-(4-chlorophenyl)-4-piperidinopteridine[36] (2.0 g, 5.3 mmol) in trifluoroacetic acid (20 mL) was shaken under H_2 atmosphere with PtO_2 (0.1 g) for 4 h until H_2 uptake was stopped. After filtration of the catalyst, the filtrate was evaporated, and the solid was treated with methanolic HCl (10%, 15 mL) for several hours. After it was evaporated, the residue was coevaporated with EtOH and then stirred in ether, filtered, and dried in a vacuum desiccator to give 1.8 g (72%) as a colorless powder; mp >170 °C (dec). UV (60% H_2SO_4): 221 (4.31), 297 (4.14). Anal. ($C_{17}H_{21}ClN_6 \times 3HCl \times H_2O$) C, H, N.

2-Amino-6-(4-methoxyphenyl)-4-piperidino-5,6,7,8-tetrahydropteridine (329). A solution of 2-amino-6-(4-methoxyphenyl)-4-piperidinopteridine[36] (0.7 g, 2 mmol) in trifluoroacetic acid (15 mL) was shaken under H_2 atmosphere with PtO_2 (0.1 g) for 24 h until H_2 uptake was stopped. It was filtered from the catalyst, the filtrate was evaporated, and the resulting solid was treated with methanolic HCL (10%, 15 mL) by stirring for several hours. After it was evaporated, the residue was coevaporated with EtOH and stirred in ether, filtered, and dried in a vacuum desiccator to give 0.7 g (74%) as a colorless powder; mp 218−220 °C (dec). UV (60% H_2SO_4): 223 (4.40), 300 (4.34). Anal. ($C_{17}H_{24}N_6O \times 3HCl \times H_2O$) C, H, N.

2-Amino-6-phenyl-4-piperidino-5,6,7,8-tetrahydropteridine (330). A solution of 2-amino-6-phenyl-4-piperidinopteridine[36] (0.6 g, 1.75 mmol) in trifluoroacetic acid (15 mL) was shaken under H_2 atmosphere with PtO_2 (0.1 g) for 4 h until H_2 was uptake stopped. It was filtered from the catalyst, the filtrate was evaporated in a vacuum, and the resulting solid was treated with methanolic HCl (10%, 15 mL) by stirring for several hours. After it was evaporated, the residue was coevaporated with EtOH and stirred in ether, filtered, and dried in a vacuum desiccator to give 0.64 g (80%) as a colorless powder; mp 178−182 °C. UV (60% H_2SO_4): 229 (4.07), 299 (4.19). Anal. ($C_{17}H_{22}N_6 \times 3HCl \times H_2O$) C, H, N.

2-Amino-6-(4-methoxyphenyl)-4-di-N-propylamino-5,6,7,8-tetrahydropteridine (332). A solution of 2-amino-6-(4-methoxyphenyl)-4-di-*n*-propylaminopteridine[36] (0.5 g, 1.35 mmol) in trifluoroacetic acid (15 mL) was shaken under H_2 atmosphere with PtO_2 (0.1 g) for 4 h until H_2 uptake was stopped. It was filtered from the catalyst, the filtrate was evaporated, and the resulting solid was treated with methanolic HCl (10%, 15 mL) by stirring for several hours. After it was evaporated, the residue was coevaporated with EtOH and stirred in ether, filtered, and dried in a vacuum desiccator to give 0.58 g (95%) as a colorless powder; mp >150 °C (dec). UV (60% H_2SO_4): 224 (4.25), 300 (4.30). Anal. ($C_{19}H_{28}N_6O \times 2HCl \times 1.5\ H_2O$) C, H, N.

2-Amino-6-(4-chlorophenyl)-4-diethylamino-5,6,7,8-tetrahydropteridine (333). A solution of 2-amino-6-(4-chlorophenyl)-4-diethylaminopteridine[36] (0.5 g, 1.52 mmol) in trifluoroacetic acid (15 mL) was shaken under H_2 atmosphere with PtO_2 (0.1 g) for 10 h until H_2 uptake was stopped. It was filtered from the catalyst, the filtrate was evaporated, and the resulting solid was treated with methanolic HCl (10%, 15 mL) by stirring for several hours. After it was evaporated, the residue was coevaporated with EtOH and then stirred in ether, filtered, and dried in a vacuum desiccator to give 0.53 g (84%) as a colorless powder; mp >220 °C (dec). UV (60% H_2SO_4): 220 (4.26), 298 (4.29). Anal. ($C_{16}H_{21}ClN_6 \times 2HC1 \times 0.5\ H_2O$) C, H, N.

2-Amino-6-(4-chlorophenyl)-4-cyclohexylmethylamino-5,6,7,8-tetrahydropteridine (334). A solution of 2-amino-6-(4-chlorophenyl)-4-dibenzylaminopteridine[36] (0.5 g, 1.06 mmol) in trifluoroacetic acid (15 mL) was shaken under H_2 atmosphere with PtO_2 (0.1 g) for 24 h until H_2 uptake was stopped. It was filtered from the catalyst, the filtrate was evaporated, and the resulting solid was treated with methanolic HCl (10%, 15 mL) by stirring for several hours. After it was evaporated, the residue was coevaporated with EtOH and stirred in ether, filtered, and dried in a vacuum desiccator to give 0.36 g (73%) as a colorless powder; mp >180 °C (dec). UV (60% H_2SO_4): 218 (4.14), 283 (4.22). Anal. ($C_{19}H_{25}ClN_6 \times 2HCl \times H_2O$) C, H, N.

5.2. Biology. Materials. L-[2,3,4,5-^{3}H]Arginine hydrochloride (>2.81 Tbq mmol^{-1}) was purchased from Amersham (Braunschweig, Germany); H_4Bip was purchased from Dr. B. Schircks Laboratories (Jona, Switzerland); β-nicotinamide adenine dinucleotide phosphate tetrasodium salt tetrahydrate (NADPH) was purchased from Applichem GmbH (Darmstadt, Germany); flavin adenine dinucleotide (FAD), flavin mononucleotide (FMN), and reduced glutathione (GSH) were purchased from Boehringer-Mannheim (Mannheim, Germany); and l-arginine hydrochloride and phosphodiesterase 3′,5′-cyclic nucleotide activator (calmodulin, CaM) were purchased from Sigma Chemicals (Deisenhofen, Germany). All other chemicals were of the highest purity available and either from Merck AG (Darmstad, Germany) or Sigma Chemicals. Water was deionized to 18 MΩ cm (Milli-Q; Millipore, Eschborn, Germany) and deoxygenated by gassing with argon.

Enzyme Activity. Native NOS-I (neuronal NOS) was isolated and purified from porcine brain cerebellum by ammonium sulfate precipitation and 2′,5′-ADP-sepharose affinity chromatography using previously described methods.[34,35] To determine NOS catalytic activity, the Ca^{2+}/calmodulin-dependent conversion of radiolabeled substrate [^{3}H]L-arginine to [^{3}H]L-citrulline was measured during a standard incubation of 15 min.[1,79] NOS-I was incubated at 37 °C in a total assay volume of 100 μL consisting of 50 nM CaM, 1 mM $CaCl_2$, 5 μM FAD, 10 μM FMN, 250 μM 3-[(3-cholamidopropyl)-dimethylammonio]-2-hydroxy-1-propanesulfonat (Chapso), 50 mM triethanolamine (TEA) buffer (pH 7.2), 1 mM NADPH, 7 mM GSH, and 50 μM L-arginine + [2,3,4,5-^{3}H]L-arginine. The reaction was stopped by adding ice-cold acetate buffer (pH 5.5). The [^{3}H]L-citrulline formed was separated by cation exchange chromatography, and the amount of radioactivity was determined by liquid scintillation counting. Total NOS-I activity was determined in the presence of saturating H_4Bip concentrations (2 μM)[34,35,79], and the effect of the antipterins was examined at an initial inhibitor concentration of 100 μM. Concentration−response curves were constructed in the range from 0 to 1000 μM. The corresponding IC_{50} values were determined by nonlinear regression analysis (fitting to sigmoidal concentration−response curves) using the UltraFit (Biosoft, Cambridge, U.K.) or Prism software (GraphPad, San Diego, CA).

Abbreviations. H_4Bip, (6*R*)-5,6,7,8-tetrahydro-L-biopterin; CoMFA, comparative molecular field analysis; IC_{50} value, concentration of inhibitor required for half-maximal inhibition; NO, nitric oxide (synonym nitrogen monoxide); NOS, nitric oxide synthase enzyme family (EC 1.14.13.39); SAR, structure−activity relationship; SCR, structurally conserved region.

Acknowledgment. This work was supported by the Bundesministerium für Bildung, Wissenschaft, Forschung und Technologie (BMBF), and Aventis (Germany). P.K. is a recipient of a C. J. Martin fellowship (Australian NH&MRC). We thank Mr. Manfred Bernhardt and Mrs. Birgit Thur for excellent technical assistance. We are particularly grateful to Drs. C. S. Raman, H. Li, P. Martásek, T. Poulos, and B. S. S. Masters for provision of structural data.

Supporting Information Available: Six additional tables with statistical results for CoMFA and CoMSIA, conformational perturbation studies, and progressive scrambling results plus four figures with comparisons of electrostatic potentials for two inhibitors, alignments and interpretations for PLS analyses for models A4 and B4 including steric, electrostatic CoMFA SD*Coeff contour maps and steric, electrostatic, and hydrophobic CoMSIA SD*Coeff contour maps. This material is available free of charge via the Internet at http://pubs.acs.org.

References

(1) Bredt, D. S.; Snyder, S. H. Isolation of nitric oxide synthetase, a calmodulin-requiring enzyme. *Proc. Natl. Acad. Sci. U.S.A.* **1990**, *87*, 682−685.

(2) Marletta, M. A. Nitric oxide synthase structure and mechanism. *J. Biol. Chem.* **1993**, *268*, 12231−12234.

(3) (a) Schmidt, H. H. H. W.; Nau, H.; Wittfoth, W.; Gerlach, J.; Prescher, K.-E.; Klein, M. M.; Niroomand, F.; Böhme, E. Arginine is a physiological precursor of endothelium-derived nitric oxide. *Eur. J. Pharmacol.* **1988**, *154*, 213−216. (b) Palmer, R. M. J.; Ashton, D. S.; Moncada, S. Vascular endothelial cells synthesize nitric oxide from L-arginine. *Nature* **1988**, *333*, 664−666.

(4) Stuehr, D. J.; Griffith, O. W. Mammalian nitric oxide synthases. In *Advances in Enzymology and Related Areas of Molecular Biology*; Meister, A., Ed.; John Wiley and Sons: New York, 1992; Vol. 65, pp 287−346.

(5) (a) Moncada, S.; Palmer, R. M. J.; Higgs, E. A. Nitric oxide: physiology, pathophysiology, and pharmacology. *Pharmacol. Rev.* **1991**, *43*, 109−142. (b) Schmidt, H. H. H. W.; Walter, U. NO at Work. *Cell* **1994**, *78*, 919−925.

(6) (a) Furchgott, R. F.; Kahn, M. T.; Jothianandan, D. Evidence supporting the proposal that endothelium-derived relaxing factor is nitric oxide. *Thromb. Res.* **1987**, *Suppl. 8*, 5. (b) Palmer, R. M. J.; Ferrige, A. G.; Moncada, S. Nitric oxide accounts for the biological activity of endothelium-derived relaxing factor. *Nature* **1987**, *327*, 524−526. (c) Ignarro, L. J.; Buga, G. M.; Wood, K. S.; et al. Endothelium-derived relaxing factor produced and released from artery and vein is nitric oxide. *Proc. Natl. Acad. Sci. U.S.A.* **1987**, *84*, 9265−9269.

(7) Crane, B. R.; Arvai, A. S.; Ghosh, D. K.; Wu, C.; Getzoff, E. D.; Stuehr, D. J.; Tainer, J. A. Structure of nitric oxide synthase oxygenase dimer with pterin and substrate. *Science* **1998**, *279*, 2121−2126.

(8) Raman, C. S.; Li, H.; Martásek, P.; Král, V.; Masters, B. S. S.; Poulos, T. L. Crystal structure of constitutive endothelial nitric oxide synthase: a paradigm for pterin function involving a novel metal center. *Cell* **1998**, *95*, 939−950.

(9) Kerwin, J. F., Jr.; Lancaster, J. R., Jr.; Feldman, P. L. Nitric oxide: A new paradigm for second messengers. *J. Med. Chem.* **1995**, *38*, 4343−4362.

(10) Griffith, O. W.; Stuehr, D. J. Nitric oxide synthases: properties and catalytic mechanism. *Annu. Rev. Physiol.* **1995**, *57*, 707−736.

(11) (a) Schmidt, H. H. H. W.; Murad, F. Purification and characterization of human NO synthase. *Biochem. Biophys. Res. Commun.* **1991**, *181*, 1372−1377. (b) Schmidt, H. H. H. W.; Pollock, J. S.; Nakane, M.; Gorsky, L. D.; Förstermann, U.; Murad, F. Purification of a soluble isoform of guanylyl cyclase-activating-factor synthase. *Proc. Natl. Acad. Sci. U.S.A.* **1991**, *88*, 365−369.

(12) Wolff, D. J.; Gribin, B. J. The inhibition of the constititive and inducible nitric oxide synthase isoforms by indazole agents. *Arch. Biochem. Biophys.* **1994**, *311*, 300−306.

(13) (a) Dawson, D. A. Nitric oxide and focal cerebral ischemia: multiplicity of actions and diverse outcome. *Cerebrovasc. Brain Metabol. Rev.* **1994**, *6*, 299−324. (b) Choi, D. W.; Rothman, S. M. The role of glutamate neuritoxicity in hypoxic-ischemic neuronal death. *Annu. Rev. Neurosci.* **1990**, *13*, 1711−182. (c) Garthwaite, J. In *The NMDA Receptor*; Watkins, J. C., Collingridge, G. L., Eds.; Oxford University Press: Oxford, England, 1989; pp 187−205.

(14) Przedborski, S.; Jackson-Lewis, V.; Yokoyama, R.; Shibata, T.; Dawson, V. L.; Dawson, T. M. Role of neuronal nitric oxide in 1-methyl-4-phenyl-1,2,3,6-tetrahydropyridine (MPTP)-induced dopaminergic neurotoxicity. *Proc. Natl. Acad. Sci. U.S.A.* **1996**, *93*, 4565−4571.

(15) (a) Moore, P. K.; Wallace, P.; Gaffen, Z.; Hart, S. L.; Babbedge, R. C. Characterization of the novel nitric oxide synthase inhibitor 7-nitro indazole and related indazoles: Antinociceptive and cardiovascular effects. *Br. J. Pharmacol.* **1993**, *110*, 219−224. (b) Thomsen, L. L.; Iversen, H. K.; Lassen, L. H.; Olesen, J. The role of nitric oxide in migraine pain. *CNS Drugs* **1994**, *2*, 417−422.

(16) (a) Förstermann, U.; Pollock, J. S.; Schmidt, H. H. H. W.; Heller, M.; Murad, F. Calmodulin-dependent endothelium-derived relaxing factor/nitric oxide synthase activity is present in the particulate and cytosolic fractions of bovine aortic endothelial cells. *Proc. Natl. Acad. Sci. U.S.A.* **1991**, *88*, 1788−1792. (b) Pollock, J. S.; Förstermann, U.; Mitchell, J. A.; Warner, T. D.; Schmidt, H. H. H. W.; Nakane, M.; Murad, F. Purification and characterization of particulate endothelium-derived relaxing factor synthase from cultured and native bovine aortic endothelial cells. *Proc. Natl. Acad. Sci. U.S.A.* **1991**, *88*, 10480−10484.

(17) MacMicking, J.; Xie, Q. W.; Nathan, C. Nitric oxide and macrophage function. *Annu. Rev. Immunol.* **1997**, *15*, 323−350.

(18) Kröncke, K. D.; Fehsel, K.; Kolb-Bachofen, V. Inducible nitric oxide synthase and its product nitric oxide, a small molecule with complex biological activities. *Biol. Chem.* **1995**, *376*, 327−343.

(19) Knowles, R. G.; Moncada, S. Nitric oxide synthases in mammals. *Biochem. J.* **1994**, *198*, 249−258.

(20) Fischmann, T. O.; Hruza, A.; Niu, X. D.; Fossetta, J. D.; Lunn, C. A.; Dolphin, E.; Prongay, A.; Reichert, P.; Lundell, D. J.; Narula, S. K.; Weber, P. C. Structural characterization of nitric oxide synthase isoforms reveals striking active-site conservation. *Nat. Struct. Biol.* **1999**, *6*, 233−242.

(21) Crane, B. R.; Arvai, A. S.; Gashhui, R.; Wu, C.; Ghosh, D. K.; Getzoff, E. D.; Stuehr, D. J.; Tainer, J. A. The structure of nitric oxide synthase oxygenase domain and inhibitor complexes. *Science* **1997**, *278*, 425−431.

(22) Wright, C. W.; Rees, D. D.; Moncada, S. Protective and pathological roles of nitric oxide in endotoxin shock. *Cardiovasc. Res.* **1992**, *26*, 48−57.

(23) Marletta, M. A. Approaches toward selective inhibition of nitric oxide synthase. *J. Med. Chem.* **1994**, *37*, 1899−1907.

(24) Olken, N. M.; Marletta, M. A. N^{γ}-methyl-L-arginine functions as an alternate substrate and mechanism-based inhibitor of nitric oxide synthase. *Biochemistry* **1993**, *32*, 9677−9685.

(25) Furfine, E. S.; Harmon, M. F.; Paith, J. E.; Garvey, E. P. Selective inhibition of constitutive nitric oxide synthase by N^{γ}-nitroarginine. *Biochemistry* **1993**, *32*, 8512−8517.

(26) McCall, T. B.; Feelisch, M.; Palmer, R. M. J.; Moncada, S. Identification of N^{δ}-iminoethyl-L-orthinine as an irreversible inhibitor of nitric oxide synthase in phagocytic cells. *Br. J. Pharmacol.* **1991**, *102*, 234−238.

(27) Huang, H.; Martasek, P.; Roman, L. J.; Masters, B. S. S.; Silverman, R. B. N^{ω}-Nitroarginine-containing dipeptide amides. Potent and highly selective inhibitors of neuronal nitric oxide synthase. *J. Med. Chem.* **1999**, *42*, 3147−3153.

(28) Hah, J.-M.; Roman, L. J.; Martásek, P.; Silverman, R. B. Reduced Amide Bond Peptidomimetics. (4*S*)-N-(4-Amino-5-[aminoalkyl]-aminopentyl)-N′-nitroguanidines, Potent and Highly Selelctive Inhibitors of Neuronal Nitric Oxide Synthase. *J. Med. Chem.* **2001**, *44*, 2667−2670.

(29) Narayanan, K.; Spack, L.; McMillan, K.; Kilbourn, R. G.; Hayward, M. A.; Masters, B. S. S.; Griffith, O. W. S-Alkyl-L-thiocitrullines. *J. Biol. Chem.* **1995**, *270*, 11103−11110.

(30) Griffith, O. W.; Gross, S. S. Inhibitors of nitric oxide synthases. In *Methods in Nitric Oxide Research*; Feelisch, M., Stamler, J. S., Eds.; John Wiley and Sons: New York, 1996; pp 187−208.

(31) Collins, J. L.; Shearer, B. G.; Oplinger, J. A.; Lee, S.; Garvey, E. P.; Salter, M.; Duffy, C.; Burnette, T. C.; Furfine, E. S. N-Phenylamidines as selective inhibitors of human neuronal nitric oxide synthase: Structure−activity studies and demonstration of in vivo activity. *J. Med. Chem.* **1998**, *41*, 2858−2871.

(32) Lowe, J. A., III; Qian, W.; Volkmann, R. A.; Heck, S.; Nowakowski, J.; Nelson, R.; Nolan, C.; Liston, D.; Ward, K.; Zorn, S.; Johnson, C.; Vanase, M.; Faraci, W. S.; Verdries, K. A.; Baxter, J.; Doran, S.; Sanders, M.; Ashton, M.; Whittle, P.; Stefaniak, M. A new class of selective and potent inhibitors of neuronal nitric oxide synthase. *Bioorg. Med. Chem. Lett.* **1999**, *9*, 2569−2572.

(33) (a) Fujisawa Pharm. Co. Ltd., WO9702254, 1997. (b) Takeda Chem Ind. Ltd., EP-0737671-A, 1996.

(34) Bömmel, H. M.; Reif, A.; Fröhlich, L. G.; Frey, A.; Hofmann, H.; Marecak, D. M.; Groehn, V.; Kotsonis, P.; La, M.; Köster, S.; Meinecke, M.; Bernhardt, M.; Weeger, M.; Ghisla, S.; Prestwich, G. D.; Pfleiderer, W.; Schmidt, H. H. H. W. Anti-Pterins as tools to characterize the function of tetrahydrobiopterin in NO synthase. *J. Biol. Chem.* **1998**, *273*, 33142−33149.

(35) Fröhlich, L. G.; Kotsonis, P.; Traub, H.; Taghavi-Moghadam, S.; Al-Masoudi, N.; Hofmann, H.; Strobel, H.; Matter, H.; Pfleiderer, W.; Schmidt, H. H. H. W. Inhibition of neuronal nitric oxide synthase by 4-amino pteridine derivatives: structure−activity relationship of antagonists of (6*R*)-5,6,7,8-tetrahydrobioperin cofactor, *J. Med. Chem.* **1999**, *42*, 4108−4121.

(36) Kotsonis, P.; Fröhlich, L. G.; Raman, C. S.; Berg, M.; Gerwig, R.; Groehn, V.; Kang, Y.; Al-Masoudi, N.; Taghavi-Moghadam, S.; Mohr, D.; Münch, U.; Schnabel, J.; Poulos, T. L.; Strobel, H.; Masters, B. S. S.; Matter, H.; Pfleiderer, W.; Schmidt, H. H. H. W. Development of novel 4-oxo pteridine antagonists of (*6R*)-5,6,7,8-tetrahydrobiopterin in neuronal nitric oxide synthase. *J. Biol. Chem.* **2001**, *276*, 49133−49141.

(37) Cramer, R. D.; Patterson, D. E.; Bunce, J. E. Comparative molecular field analysis (CoMFA). 1. Effect of shape on binding of steroids to carrier proteins. *J. Am. Chem. Soc.* **1988**, *110*, 5959−5967.

(38) Clark, M.; Cramer, R. D.; Jones, D. M.; Patterson, D. E.; Simeroth, P. E. Comparative molecular field analysis (CoMFA). 2. Towards its use with 3D-structural databases. *Tetrahedron Comput. Methodol.* **1990**, *3*, 47−59.

(39) *3D-QSAR in Drug Design. Theory, Methods and Applications*; Kubinyi, H., Ed.; ESCOM: Leiden (NL), 1993.

(40) Klebe, G.; Abraham, U.; Mietzner, T. Molecular similarity indices in a comparative analysis (CoMSIA) of drug molecules to correlate and predict their biological activity. *J. Med. Chem.* **1994**, *37*, 4130−4146.

(41) (a) Wold, S.; Albano, C.; Dunn, W. J.; Edlund, U.; Esbenson, K.; Geladi, P.; Hellberg, S.; Lindberg, W.; Sjöström, M. In *Chemometrics: Mathematics and Statistics in Chemistry*; Kowalski, B., Ed.; Reidel: Dortrecht, The Netherlands, 1984; pp 17−95. (b) Dunn, W. J.; Wold, S.; Edlund, U.; Hellberg, S.; Gasteiger, J. Multivariate structure−activity relationship between data from a battery of biological tests and an ensemble of structure descriptors: The PLS method. *Quant. Struct.-Act. Relat.* **1984**, *3*, 31−137. (c) Geladi, P. Notes on the history and nature of Partial Least Squares (PLS) modelling. *J. Chemom.* **1988**, *2*, 231−246.

(42) (a) Wold, S. Cross-validatory estimation of the number of component in factor and principal component models. *Technometrics* **1978**, *4*, 397−405. (b) Diaconis, P.; Efron, B. Computer-intensive methods for statistics. *Sci. Am.* **1984**, *116*, 96−117. (c) Cramer, R. D.; Bunce, J. D.; Patterson, D. E. Crossvalidation, bootstrapping and partial least squares compared with multiple regression in conventional QSAR studies. *Quant. Struct.-Act. Relat.* **1988**, *7*, 18−25.

(43) *SYBYL Molecular Modelling Package*, version 6.5; Tripos: St. Louis, MO, 1999.

(44) Clark, M.; Cramer, R. D.; Van Opdenbosch, N. Validation of the General Purpose Tripos 5.2 Force Field. *J. Comput. Chem.* **1989**, *10*, 982−1912.

(45) Gasteiger, J.; Marsili, M. Iterative partial equalization of orbital electronegativity: a rapid access to atomic charges. *Tetrahedron* **1980**, *36*, 3219−3228.

(46) Stewart, J. J. P.; Seiler, F. J. *MOPAC*, version 6.0; QCPE program No. 455, Quantum Chemistry Program Exchange, University of Indiana: Bloomington, IN, 1989. Used as implemented in *Sybyl* 6.5.; Tripos: St. Louis, MO, 1998.

(47) Dewar, M. J. S.; Zoebisch, E. G.; Healy, E. F.; Stewart, J. J. P. Development and use of quantum mechanical molecular models. 76. AM1: a new general purpose quantum mechanical molecular model. *J. Am. Chem. Soc.* **1985**, *107*, 3902−3907.

(48) PDB files obtained from Protein Database (National Brookhaven Laboratories): 1noc, 1nos, 2nos, 1nod, 2nod, 3nod (http://www.pdb.bnl.gov). Bernstein, F. C.; Koetzle, T. F.; Williams, G. J. B.; Meyer, E. F.; Brice, M. D.; Rodgers, J. R.; Kennard, O.; Shimanouchi, T.; Tasumi, M. The Protein Data Bank: a computer-based archival file for macromolecular structures. *J. Mol. Biol.* **1977**, *112*, 535−542.

(49) Goodford, P. J. A computational procedure for determining energetically favorable binding sites on biologically important macromolecules. *J. Med. Chem.* **1985**, *28*, 849−857.

(50) (a) Heiden, W.; Goetze, T.; Brickmann, J. Fast generation of molecular surfaces from 3D data fields with enhanced 'marching cube' algorithm. *J. Comput. Chem.* **1993**, *14*, 246−250. (b) Brickmann, J.; Bertling, H.; Bussian, B. M.; Goetze, T.; Knoblauch, M.; Waldherr-Teschner, M. MOLCAD − interactive molecular computer graphics on high-performance computers. *Tagungsber.-Vortragstag., Ges. Dtsch. Chem., Fachgruppe Chem.-Inf.* **1987**, 93−111. (c) Implemented in *SYBYL* 6.5; Tripos: St. Louis, MO, 1999.

(51) Heiden, W.; Moeckel, G.; Brickmann, J. A new approach to the display of local lipophilicity/hydrophilicity mapped on molecular surfaces. *J. Comput.-Aided Mol. Des.* **1993**, *7*, 503−514.

(52) (a) Ghose, A.; Crippen, G. Atomic physicochemical parameters for three-dimensional structure-directed quantitative structure−activity relationships. 1. Partition coefficients as a measure of hydrophobicity. *J. Comput. Chem.* **1986**, *7*, 565−577. (b) Viswanadhan, V. N.; Ghose, A. K.; Revankar, G. R.; Robins, R. K. Atomic physicochemical parameters for three-dimensional structure-directed quantitative structure−activity relationships. 4. Additional parameters for hydrophobic and dispersive interactions and their application for an automated superposition of certain naturally occurring nucleoside antibiotics. *J. Chem. Inf. Comput. Sci.* **1989**, *29*, 163−172.

(53) (a) Klapper, I.; Hagstrom, R.; Fine, R.; Sharp, K.; Honig, B. Focusing of electric fields in the active site of copper−zinc superoxide dismutase: effects of ionic strength and amino acid modification. *Proteins* **1986**, *1*, 47−59. (b) Nicholls, A.; Honig, B. A rapid finite difference algorithm, utilizing successive over-relaxation to solve the Poisson−Boltzmann equation. *J. Comput. Chem.* **1991**, *12*, 435−445. (c) Gilson, M.; Sharp, K.; Honig, B. Calculating the electrostatic potential of molecules in solution: method and error assessment. *J. Comput. Chem.* **1988**, *9*, 327−335.

(54) (a) Connolly, M. L. Solvent-accessible surfaces of proteins and nucleic acids. *Science* **1983**, *221*, 709−713. (b) Connolly, M. L. Analytical molecular surface calculation. *J. Appl. Crystallogr.* **1983**, *16*, 548−558.

(55) (a) Blundell, T. L.; Carney, D. P.; Gardner, S.; Hayes, F. R. F.; Howlin, B.; Hubbard, T. J. P.; Overington, J. P.; Singh, D. A.; Sibanda, B. L. Sutcliffe, M. J. Knowledge-based protein modeling and design. *Eur. J. Biochem.* **1988**, *172*, 513−520. (b) Sutcliffe, M. J.; Haneef, I.; Carney, D. P.; Blundell, T. L. Knowledge-based modeling of homologous proteins. Part I: Three-dimensional frameworks derived from the simultaneous superposition of multiple structures. *Protein Eng.* **1987**, *1*, 377−384. (c) Sutcliffe, M. J.; Hayes, F. R. F.; Blundell T. L. Knowledge based modeling of homologous proteins. Part II: Rules for the conformations of substituted side chains. *Protein Eng.* **1987**, *1*, 385−392.

(56) Srinivasan, N.; Blundell, T. An evaluation of the performance of an automated procedure for comparative modelling of protein tertiary structure. *Protein Eng.* **1993**, *6*, 501−512.

(57) The UNITY 4.0 version of the CSD database was used; CSD-UNITY version 5.15, April 1998. Cambridge Crystallographic Data Centre CCDC, 12, Union Road, Cambridge CB2, 1EZ, U.K.

(58) (a) Jones, G.; Willett, P.; Glen, R. C. A genetic algorithm for flexible molecular overlay and pharmacophore elucidation. *J. Comput.-Aided Mol. Des.* **1995**, *9*, 532−549. (b) GASP available from Tripos, St. Louis, MO, 1999.

(59) Krömer, R. T.; Hecht, P. A new procedure for improving the predictiveness of CoMFA models and its application to a set of dihydrofolate reductase inhibitors. *J. Comput.-Aided Mol. Des.* **1995**, *9*, 396−406.

(60) Dove, S.; Buschauer, A. Improved alignment by weighted field fit in CoMFA of histamine H_2 receptor agonistic imidazolylpropylguanidines. *Quant. Struct.-Act. Relat.* **1999**, *18*, 329−341.

(61) Kearsley, S. K.; Smith, G. M. An alternative method for the alignment of molecular structures: Maximizing electrostatic and steric overlap. *Tetrahedron Comput. Methodol.* **1990**, *3*, 615−633.

(62) (a) Thibaut, U.; Folkers, G.; Klebe, G.; Kubinyi, H.; Merz, A.; Rognan, D. Recommendations for CoMFA studies and 3D QSAR publications. In *3D QSAR in Drug Design. Theory, Methods and Applications*; Kubinyi, H., Ed.; ESCOM: Leiden, The Netherlands, 1993; pp 711−717. (b) Folkers, G.; Merz, A.; Rognan, D. CoMFA: Scope and limitations. In *3D QSAR in Drug Design. Theory, Methods and Applications*; Kubinyi, H., Ed.; ESCOM: Leiden, The Netherlands, 1993; pp 583−616. (c) Cramer, R. D.; DePriest, S. A.; Patterson, D. E.; Hecht, P. The developing practice of comparative molecular field analysis. In *3D QSAR in Drug Design. Theory, Methods and Applications*; Kubinyi, H., Ed.; ESCOM: Leiden, The Netherlands, 1993; pp 443−485.

(63) Sheridan, R. P.; Nachbar, R. B.; Bush, B. L. Extending the trend vector: The trend matrix and sample-based partial least squares. *J. Comput.-Aided Mol. Des.* **1994**, *8*, 323−340.

(64) Clark, M.; Cramer, R. D. The probability of chance correlation using partial least squares (PLS). *Quant. Struct.-Act. Relat.* **1993**, *12*, 137−145.

(65) Leonard, J. M.; Clark, R. D. PLS Validation by progressive scrambling. Poster at the 12th European Symposium on Quantitative Structure−Activity Relationships (QSAR 1998).

(66) (a) Yan, X.; Hollis, T.; Svinth, M.; Day, P.; Monzingo, A. F.; Milne, G. W. A.; Robertus, J. D. Structure-based identification of a ricin inhibitor. *J. Mol. Biol.* **1997**, *266*, 1043−1049. (b) Birdsall, D. L.; Finer-Moore, J.; Stroud, R. M. Entropy in bisubstrate enzymes: proposed role of an alternate site in chaperoning substrate into, and products out of, thymidylate synthase. *J. Mol. Biol.* **1996**, *255*, 522−535.

(67) Werner-Felmayer, G.; Gross, S. S. Analysis of Tetrahydrobiopterin and Its Role in Nitric Oxide Synthesis. In *Methods in Nitric Oxide Research*; Feelisch, M., Stamler, J. S., Eds.; Wiley: New York, 1997; pp 271−299.

(68) Pötter, T.; Matter, H. Random or Rational Design? Evaluation of Diverse Compound Subsets from Chemical Structure Databases. *J. Med. Chem.* **1998**, *41*, 478−488.

(69) Lajiness, M.; Johnson, M. A.; Maggiora, G. M. Implementing Drug Screening Programs using Molecular Similarity Methods. In *QSAR: Quantitative Structure−Activity Relationships in Drug Design*; Fauchere, J. L., Ed.; Alan R. Liss Inc.: New York, 1989; pp 173−176.

(70) Taylor, R. Simulation Analysis of Experimental Design Strategies for Screening Random Compounds as Potential New Drugs and Agrochemicals. *J. Chem. Inf. Comput. Sci.* **1995**, *35*, 59−67.

(71) Böhm, M.; Stürzebecher, J.; Klebe, G. Three-Dimensional Quantitative Structure−Activity Relationship Analyses Using Comparative Molecular Field Analysis and Comparative Molecular Similarity Indices Analysis To Elucidate Selectivity Differences of Inhibitors Binding to Trypsin, Thrombin, and Factor Xa. *J. Med. Chem.* **1999**, *42*, 458−477.

(72) Lemmen, C.; Lengauer, T.; Klebe, G. FLEXS: A Method for Fast Flexible Ligand Superposition. *J. Med. Chem.* **1998**, *41*, 4502−4520.

(73) (a) Duffy, E. M.; Jorgensen, W. L. Prediction of Properties from Simulations: Free Energies of Solvation in Hexadecane, Octanol, and Water. *J. Am. Chem. Soc.* **2000**, *122*, 2878−2888. (b) Jorgensen, W. L.; Duffy, E. M. Prediction of drug solubility from Monte Carlo simulations. *Bioorg. Med. Chem Lett.* **2000**, *10*, 1155−1158. (c) QikProp version 1.5 available from Schrödinger, Inc., 1500 SW First Ave., Suite 1180, Portland, OR.

(74) (a) Filipponi, E.; Cecchetti, V.; Tabarrini, O.; Bonelli, D.; Fravolini, A. Chemometric rationalization of the structural and physicochemical basis for selective cyclooxygenase-2 inhibition: toward more specific ligands. *J. Comput.-Aided Mol. Des.* **2000**, *14*, 277−291. (b) Talley, J. J. Selective inhibitors of cyclooxygenase-2 (COX-2). *Prog. Med. Chem.* **1999**, *36*, 201−234. (c) Matter, H.; Schwab, W. Affinity and selectivity of matrix metalloproteinase inhibitors: A chemometrical study from the perspective of ligands and proteins. *J. Med. Chem.* **1999**, *42*, 4506−4523. (d) Pastor, M.; Cruciani, G. A novel strategy for improving ligand selectivity in receptor-based drug design. *J. Med. Chem.* **1995**, *36*, 4637−4647.

(75) Groehn, V.; Fröhlich, L. G.; Schmidt, H. H. H. W.; Pfleiderer, W. Pteridine-Based Photoaffinity Probes for Nitric Oxide Synthase and Aromatic Amino Acid Hydroxylases. *Helv. Chim. Acta* **2000**, *83*, 2738−2750.

(76) Pfleiderer, W.; Zondler, H. Pteridine, XXXI. Synthese und Eigenschaften blockierter 7,8-Dihydro-pterine. *Chem. Ber.* **1966**, *99*, 3008−3021.

(77) Traub, H.; Pfleiderer, W. Pteridines CX. Synthesis and properties of 6-substituted 2,4-diaminopteridines and pterins. *Pteridines* **1999**, *10*, 79−90.

(78) Mohr, D.; Kazimierczuk, Z.; Pfleiderer, W. Pteridines. Part XCVII. Synthesis and properties of 6-thioxanthopterin and 7-thioisoxanthopterin. *Helv. Chim. Acta* **1992**, *75*, 2317−2326.

(79) Hofmann, H.; Schmidt, H. H. H. W. Thiol dependence of nitric oxide synthase. *Biochemistry* **1995**, *34*, 13443−13452.

JM020074G